Latest Permian carbonate-carbon isotope variability traces heterogeneous organic carbon accumulation and authigenic carbonate formation

Martin Schobben[1,2], Sebastiaan van de Velde[3], Jana Suchocka[2], Lucyna Leda[2], Dieter Korn[2],
Ulrich Struck[2], Clemens Vinzenz Ullmann[4], Vachik Hairapetian[5], Abbas Ghaderi[6], Christoph Korte[7],
Robert J. Newton[1], Simon W. Poulton[1], and Paul B. Wignall[1]

[1]School of Earth and Environment, University of Leeds, Woodhouse Lane, Leeds, LS2 9JT, United Kingdom
[2]Museum für Naturkunde, Leibniz-Institut für Evolutions- und Biodiversitätsforschung, Invalidenstr. 43, D-10115 Berlin, Germany
[3]Analytical, Environmental and Geochemistry, Vrije Universiteit Brussel, Pleinlaan 2, 1050, Brussels, Belgium
[4]College of Engineering,Mathematics and Physical Sciences, Camborne School of Mines, University of Exeter, Penryn Campus, Penryn, Cornwall TR10 9FE, United Kingdom
[5]Department of Geology, Khorasgan (Esfahan) Branch, Islamic Azad University, P.O. Box 81595-158, Esfahan, Iran
[6]Department of Geology, Faculty of Sciences, Ferdowsi University of Mashhad, Mashhad, Iran
[7]Department of Geosciences and Natural Resource Management, University of Copenhagen, ØsterVoldgade 10, DK-1350 Copenhagen, Denmark

Correspondence to: Martin Schobben (m.schobben@leeds.ac.uk or schobbenmartin@gmail.com)

Abstract. Bulk-carbonate carbon isotope measurements are a widely applied proxy for investigating the ancient biogeochemical carbon cycle. Temporal carbon isotope trends serve as a prime stratigraphic tool, with the inherent assumption that bulk micritic carbonate rock is a faithful geochemical recorder of the isotopic composition of seawater dissolved inorganic carbon. However, bulk-carbonate rock is also prone to incorporate diagenetic signals. The aim of the present study is to disentangle
5 primary trends from diagenetic signals in carbon isotope records which traverse the Permian–Triassic boundary in marine carbonate-bearing sequences of Iran and South China. By pooling newly produced and published carbon isotope data we confirm that a global first-order trend towards depleted values exists. However, a large amount of scatter is superimposed on this geochemical record. In addition, we observe a temporal trend in the amplitude of this residual δ^{13}C variability, which is reproducible for the two studied regions. We suggest that (sub)seafloor microbial communities and their control on calcite nu-
10 cleation as well as on ambient porewater dissolved inorganic carbon-δ^{13}C pose a viable mechanism to induce bulk-rock δ^{13}C variability. Numerical model calculations highlight that early diagenetic carbonate rock stabilization, and linked carbon isotope alteration, can be controlled by organic matter supply and subsequent microbial remineralization. Low marine sulfate and a major biotic decline among late Permian bottom-dwelling organisms facilitated a spatial increase in heterogeneous organic carbon accumulation, causing varying degrees of carbon isotope overprint. A simulated time series suggests that a 50% increase
15 in the spatial scatter of organic carbon relative to the average, in addition to an imposed increase in the likelihood of sampling cements formed by microbial calcite nucleation to one out of 10 samples, is sufficient to induce the observed signal of carbon isotope variability. These findings put constraints on the application of Permian-Triassic carbon isotope chemostratigraphy

based on whole-rock samples, which appears less refined than classical biozonation dating schemes. On the other hand, this signal of increased carbon isotope variability concurrent with the largest mass extinction of the Phanerozoic may inform about local carbon cycling mediated by spatially heterogeneous (sub)-seafloor microbial communities under suppressed bioturbation.

1 Introduction

5 Carbon isotopes in carbonate rock are a pivotal tool for understanding the ancient biogeochemical carbon cycle, as well as a stratigraphic aid in determining the age of sedimentary deposits. Individual fossil carbonate shells are the preferred recorder of the isotope composition of marine dissolved inorganic carbon (DIC). However, some deposits, such as those of Precambrian age, or those which were formed during biotic crises or where shelly fossils are absent, are not suitable for such a single-component approach (Veizer et al.; Prokoph et al., 2008). Under these circumstances, bulk-rock samples are a widely

10 used alternative recorder (Saltzman, 2001; Brand et al., 2012a, b). This approach has attracted criticism due to the complex multicomponent nature and high potential for diagenetic alteration, which may result in a mixture of primary and secondary diagenetic signals. Major sources of contamination that are known to affect the primary marine carbon isotope signal of bulk-carbonate rock are degradation of organic matter, methanogenesis and methane oxidation (Marshall, 1992; Reitner et al., 2005; Wacey et al., 2007; Birgel et al., 2015).

15 Carbonate sediments are especially prone to chemical alteration during early compaction and lithification, when the highly porous sediment and unstable carbonate polymorphs (e.g., aragonite and high-Mg calcite) are subjected to cementation and dissolution (Bathurst, 1975; Irwin et al., 1977; Marshall, 1992). The potential for diagenetic alteration of biogenic high-Mg calcite and aragonite results from elevated substitution of foreign ions in the lattice and a higher degree of dislocations (Busenberg and Plummer, 1989). Under marine conditions, this reactive and biologically active section of the sediment column can

20 be envisioned to leave an imprint on carbonate chemistry, including the carbon isotope composition. This carbon isotope signal will be retained in post-depositional carbonate cements, and is controlled by organic carbon (OC) fluxes, pH, alkalinity, and the nature of the (sub)-seafloor microbial communities (Reitner et al., 2005; Wacey et al., 2007; Birgel et al., 2015; Zhao et al., 2016). Alternatively, on carbonate platforms subjected to rapid sea level fluctuations, lithification might be controlled by interaction with meteoric fluids and oxidized terrestrial organic matter (Brand and Veizer, 1980, 1981; Banner and Hanson, 1990;

25 Knauth and Kennedy, 2009).

A more nuanced view on the nature of bulk-rock carbon isotope composition would be to envision diagenetic overprinting on carbonate rock chemistry as a spectrum, where pure primary and strictly diagenetic endmember states are considered as a continuum, with bulk-rock chemistry falling somewhere in between these two extremes (cf. Marshall, 1992). In this case, the aim should be to discern the degree to which an original imprint could have been retained in the bulk-rock signal. Embracing

30 both ends of this spectrum could illuminate new aspects of marine sedimentary systems and ancient ocean chemistry, as well as providing a more-refined understanding of the mechanisms that promote the diagenetic alteration of carbonate sediments. Clear examples of the importance of interpreting diagenetic signals have been given by the assertion that authigenic carbonate

production might play a primary role in the global biogeochemical carbon cycle (Schrag et al., 2013), and in the isotopic imprint of terrestrial biomass on Precambrian carbonates (Knauth and Kennedy, 2009).

2 Background: Permian–Triassic carbonate-carbon isotope records

Temporal trends in carbonate-carbon isotope composition have been recorded at varying time-scales, from million-year sec-
5 ular trends (Veizer et al.; Zachos et al., 2001) to dramatic submillion year events, such as at the Paleocene Eocene Thermal Maximum (Dickens et al., 1995). The sedimentary record of the Permian–Triassic (P–Tr) boundary interval, marked by the largest mass extinction of the Phanerozoic (Erwin, 1993; Alroy et al., 2008), is also characterised by pronounced carbon isotope excursions, which are almost exclusively recorded in bulk-rock. However, chemical signatures from this time period include records with a wide variety of amplitudes and shapes, and span centimetres to metres of rock sequence (e.g., Xie et al., 2007;
10 Korte et al., 2010). Equally diverse are the proposed drivers of these geochemical signals, ranging from prolonged episodes of volcanism, eustatic-controlled erosion of organic-rich shelf sediments, to abrupt blooms of methane-producing microbes (Renne et al., 1995; Berner, 2002; Rothman et al., 2014).

Variable amplitude carbon isotope excursions in shelf to basin transects have been linked to an intensified biological pump (Meyer et al., 2011; Song et al., 2013). This notion contrasts with the viewpoint of collapsed primary productivity (or a
15 "Strangelove Ocean") as a driver for the demise of bottom-dwelling and infaunal marine biota (Rampino and Caldeira, 2005). The loss of these geobiological agents resulted in a reduced thickness of the sedimentary mixed layer and a global increase in the occurrence of laminated sediments (Wignall and Twitchett, 1996; Hofmann et al., 2015). Contrary to disrupted primary productivity, these geological features would also agree with a scenario of enhanced OC remineralization and resulting widespread marine de-oxygenation (Meyer et al., 2008, 2011). These contrasting scenarios of global-scale environmental deterioration are
20 difficult to reconcile. Nevertheless, the reduction of sediment mixing is an unequivocal feature, that warrants consideration when interpreting P–Tr chemical records.

High carbonate ion concentrations are a predicted aspect of an ocean without pelagic calcifiers, which only started proliferating during the Mesozoic, and would effectively buffer short-term perturbations to P–Tr marine carbon isotopes (Kump and Arthur, 1999; Zeebe and Westbroek, 2003; Rampino and Caldeira, 2005). This does not, however, exclude local departures
25 from this dynamic equilibrium or depth-related isotope differences, such as those forced by the biological pump (Kump and Arthur, 1999; Rampino and Caldeira, 2005). High carbonate ion concentrations are also invoked to explain the advent of (microbial) carbonate seafloor structures (e.g., thrombolites, stromatolites and fan-shaped structures) in the extinction aftermath and the ensuing Early Triassic recovery phase (Baud et al., 1997; Rampino and Caldeira, 2005; Riding and Liang, 2005; Pruss et al., 2006; Kershaw et al., 2007, 2009; Leda et al., 2014). While conditions favoured the formation of these structures, poorly
30 buffered calcified metazoans (e.g., brachiopods and corals) were proportionally more affected by the end-Permian mass extinction (Knoll et al., 2007). This biotic shift has been interpreted as a prevalent carbonate factory turnover, from skeletal to microbial (e.g., Kershaw et al., 2009).

A carbonate factory turnover, reduced sediment mixing and increased OC sinking fluxes invite consideration of a scenario where these individual parameters act as synergistic effects on carbonate formation and diagenetic stabilization. Moreover, the imprint of ^{12}C-depleted carbon on latest Permian carbonate rock by the introduction of authigenic carbonate has been connected to a systematic carbon isotope offset between bulk-rock and brachiopod shells (Schobben et al., 2016). Authigenic

5 carbonate sources can, however, result in a range of carbon isotope values, relating to the specific microbial community and sedimentary environment (Irwin et al., 1977). Hence, we hypothesize that spatial carbon isotope variability at the P–Tr boundary interval relates to an increased importance of microbially controlled calcite nucleation (i.e., *the diagenetic C isotope recorder*). Moreover, we postulate that organic carbon sinking fluxes and subsequent *in situ* remineralization by microbes determine the trajectory of carbonate rock stabilization (i.e., *the carbon source*). Combined geographic-differential OC sinking fluxes (km-

10 scale) and sediment mixing (cm-scale) might have generated spatially heterogeneous dispersion of organic carbon. This spatial pattern of OC distribution links to observed carbonate carbon isotope variability by modulating the chance of sampling variable isotope signals along lateral lithological transects (i.e., *sediment OC homogeneity*). We adopt this conceptual model as a working hypothesis for interpreting stratigraphic carbon isotope patterns in P–Tr carbonate rock. In addition, however, this scenario likely has implications for the interpretation of bulk-rock carbon isotope patterns during other periods of the Precambrian and

15 Phanerozoic.

To carry out this investigation, we study carbonate-bearing sequences of Permian to Triassic strata located in Iran and China, in combination with a compilation of published data. The effect of microbial metabolism on sediments and porewater can be numerically approximated by reactive-transport models (Soetaert et al., 1996; Boudreau, 1997; Meysman et al., 2003; van de Velde and Meysman, 2016). Similarly, diagenetic models have proven useful in delineating trajectories of bulk-rock Sr and Ca

20 isotope stabilization (Fantle and DePaolo, 2006, 2007). For the purpose of our study, we will combine aspects of these models in an effort to estimate the potential for microbially mediated spatial modification of bulk-rock carbon isotope signals.

3 Materials and methods

3.1 Bulk-carbonate carbon isotope records

3.1.1 Material selection and stable carbon isotope measurements

25 The P–Tr limestone sequences of Iran are particularly suited to study spatial $\delta^{13}C_{carb}$ variations, as lateral lithological homogeneity excludes a strong control from paleoceanographic conditions or selective preservation potential (Supplementary Information). Besides the classical P–Tr sites of, e.g., Shahreza, Zal and Ali Bashi of Iran, we sampled several other sites, for which we present the first $\delta^{13}C_{carb}$ results. These sites include the Aras Valley profile (39.015°N, 45.434°E) about 19 km WNW of the towns of Dzhulfa (Azerbaijan) and Julfa (Iran), four parallel sections in the Baghuk mountains (section A:

30 31.563°N, 52.438°E; section 1: 31.567°N, 52.444°E; section C: 31.567°N, 52.443°E; section J: 31.565°N, 52.441°E) 50 km NNW of Abadeh and 140 km SSE of Esfahan, as well as the Asadabad succession (31.848°N, 52.181°E). Limestone, marl-

stone and calcareous shale (>20 % $CaCO_3$) beds were collected bed-by-bed. Powder aliquots were produced by microdrilling fresh rock surfaces to avoid sampling of obvious late diagenetic calcite veins and weathered surfaces.

A total of 463 stable carbon isotope measurements were made at the University of Copenhagen (UC) and the Museum für Naturkunde (MfN), Berlin. Glass reaction vessels (LABCO®) containing the sample powders were flushed with helium, and
5 carbonate was left to react with 50 (UC) or 30 (MfN) µl of anhydrous phosphoric acid (102 %), for at least 1.5 h. Carbon and oxygen isotope values were measured from resulting CO_2 using an IsoPrime triple collector Isotope Ratio Mass Spectrometer in continuous flow setup (UC) or a Thermo Finnigan Gasbench (GS) II linked to a THERMO/Finnigan MAT V isotope ratio mass spectrometer (IRMS) (MfN). Pure CO_2 (99.995 %), calibrated against international IAEA standards (NSB-18 and NSB-19), was used as a reference gas. At the UC, results were corrected for weight-dependent isotope ratio bias using multiple
10 measurements of an in-house standard LEO (Carrara Marble, $\delta^{13}C$ = 1.96 ‰) covering the entire range of signal intensities encountered in the samples. External reproducibility was monitored by replicate analysis of the in-house standards LEO and Pfeil STD (Solnhofen Limestone), at the UC and MfN respectively. Long-term precision was better than 0.1 ‰ ($2\,\sigma$) (and better than 0.2 ‰ $2\,\sigma$ for oxygen isotopes). All carbon isotope values are reported in ‰ relative to VPDB, and in standard δ-notation.

3.1.2 Complementary data collection

15 Our new data are complemented by published bulk-carbonate $\delta^{13}C$ data from multiple P–Tr localities in Central Iran (Abadeh (Heydari et al., 2000; Korte et al., 2004b; Horacek et al., 2007; Korte et al., 2010; Liu et al., 2013) and Shahreza (Korte et al., 2004a; Heydari et al., 2008; Richoz et al., 2010), as well as Northwest Iran (Ali Bashi mountains and Zal; Baud et al., 1989; Korte et al., 2004c; Korte and Kozur, 2005; Kakuwa and Matsumoto, 2006; Horacek et al., 2007; Richoz et al., 2010; Schobben et al., 2016). For a more global perspective and comparative approach, we additionally extracted published data from the P–Tr
20 Global Stratigraphic Section and Point (GSSP) at Meishan, China (Baud et al., 1989; Chen et al., 1991; Xu and Yan, 1993; Hoffman et al., 1998; Jin et al., 2000; Cao et al., 2002; Gruszczyński et al., 2003; Zuo et al., 2006; Kaiho et al., 2006; Huang et al., 2007; Riccardi et al., 2007; Xie et al., 2007). Data was extracted from tables and supplementary files or provided by the authors, and where necessary read from figures with the open-source software *xyscan* (Ullrich, 2016). This compilation adds 2077 data points to our new dataset. The analytical uncertainty of the collected data, when given, ranges between 0.02 and
25 0.2 ‰. We included replicate studies on the same site, as this data is potentially a valuable asset to test the reproducibility of stable isotope investigations and to shed light on the effect of the bulk-rock multicomponent nature on $\delta^{13}C_{carb}$ composition.

3.1.3 Data projection

To facilitate a direct comparison of $\delta^{13}C_{carb}$ between different sites with differences in total sediment thickness, we converted the stratigraphic height to a dimensionless timeline. This approach preserves a more direct connection to the sampled rock
30 sequence, rather than converting to absolute ages or maintaining original stratigraphic heights. The conversion to a dimensionless time grid was carried out by using the lower and upper bounds of individual conodont assemblage biozones as tie-points to which a relative distance for an individual $\delta^{13}C_{carb}$ datapoint is assigned (Supplementary Information). The chronological

Table 1. Correlative biostratigraphic units

Unit	Iran	China*
K	*Neospathodus dieneri*	*Stepanovites kummeli*
J	*Hindeodus postparvus*	*Clarkina tulongensis-Clarkina planata*
I	*Isarcicella isarcica*	*Isarcicella isarcica*
	Isarcicella staeschei	*Isarcicella staeschei*
H	*Hindeodus lobata*	
	Hindeodus parvus	*Hindeodus parvus*
G	*Merrillina ultima - Stepanovites mostleri*	
	Hindeodus praeparvus - Hindeodus changxingensis	*Hindeodus changxingensis*
F	*Clarkina hauschkei*	
	Clarkina abadehensis	*Clarkina meishanensis*
E	*Clarkina yini*	*Clarkina yini*
	Clarkina nodosa	
	Clarkina bachmanni	
D	*Clarkina changxingensis*	*Clarkina changxingensis*
C	*Clarkina subcarinata*	*Clarkina wangi - Clarkina subcarinata*
B	*Clarkina orientalis*	*Clarkina orientalis*
A	*Clarkina trancaucasica*	
	Clarkina leveni	

* Meishan P–Tr GSSP. See the Supplementary Information file for references regarding the biostratigraphical studies considered to construct this biozonation scheme.

scheme used here divides the P–Tr interval into biostratigraphic units (A–K), which enables correlation of individual sequences of both geographic regions (Table 1).

To evaluate trends in the collected data, a sliding window with a bandwidth equivalent to the dimensionless grid unit has been applied to the $\delta^{13}C_{carb}$ data. This method ensures the extraction of temporal trends at equivalent time resolution to the biozonation units. To cancel out the potential for an uneven spread of data points we also applied a subsampling routine on the Iranian and Chinese datasets. Subsampling was performed with the sliding window procedure, as described above, before applying summary statistics. Subsequently, the median values were calculated for each of subsampled $\delta^{13}C_{carb}$ population. For simplification, the resulting median trend line and 95 % confidence intervals (CI) are calculated and visually weighted (cf. "Visually Weighted Plot" or "Watercolor Regression"; Hsiang, 2012; Schönbrodt, 2012). The latter is accomplished by calculating a kernel density, and both the drawn median trend line and CI interval are weighted by colour saturation, based on this kernel density value. In addition, the median trend line and the CI interval have been assigned contrasting colours to further enforce the visual signal. Hence, saturated and contrasting parts of the depicted regression curve (i.e., sections with high visual weight) depict areas with the highest fidelity of the temporal geochemical pattern, based on the subsampling routine. In

addition to the median trend lines, the same subsampling approach and visual weighting has been applied to calculate and plot the interquartile range (IQR; the value-range containing 50 % of the sample-population) and 95 %-interpercentile range (IPR; the value-range containing 95 % of the sample-population). Graphs are plotted with the open-source programming platform R (R Core Team, 2016) and with the aid of the R packages; *ggplot2* (Wickham, 2009), *reshape2* (Wickham, 2007), *plyr*
5 (Wickham, 2011) and *gridExtra* (Auguie, 2016).

3.2 Reactive-transport modelling

3.2.1 Geochemical model formulation and biogeochemical reactions

Organic matter availability fuels *in situ* metabolic pathways linked to calcite nucleation, relying on electron acceptors, e.g., (listed in order of free energy gain) O_2, SO_4^{2-} and eventually organic matter. Although significant overlap occurs, depletion of
10 the thermodynamically most favourable energy acceptor allows consumption of the less energy yielding species in line, leading to redox zonation in the sediment (Berner, 1964; Froelich et al., 1979). Combined with the metabolism-specific carbon isotope signature of DIC introduced to the porewater, this creates a potential source for diagenetic alteration of carbonate-C isotope signatures (Irwin et al., 1977).

Depth profiles for bio-reactive elements can be described by mass balance equations (equations 1 and 2), which can subse-
15 quently be solved numerically via the *method-of-lines* (Boudreau, 1997; Soetaert and Meysman, 2012). The numerical solutions of these equations solve the age–depth (t and z) relationship of deposited sediments in terms of solids (S_i), as well as solutes (C_i) in pore fluids, and their respective reactions between the solid and liquid phase. At the top of the sediment pile the porewaters communicate with ocean water so that dissolved elements can diffuse according to their concentration gradients. Besides diffusion transport processes, continued sedimentation supplies the sediment with organic carbon and calcium carbonate.

$$20 \quad \varphi \frac{\partial C_i}{\partial t} = \frac{\partial}{\partial z}\left(\varphi D_i \frac{\partial C_i}{\partial z} - \varphi \nu C_i\right) + \sum_k \nu_{i,k} R_k \tag{1}$$

$$(1-\varphi)\frac{\partial S_i}{\partial t} = \frac{\partial}{\partial z}\left((1-\varphi)D_b(z)\frac{\partial S_i}{\partial z} - (1-\varphi)wS_i\right) + \sum_k \nu_{i,k} R_k \tag{2}$$

The equations to describe the reactive-transport model have two transport parameters: molecular diffusion of solutes (D_0) and sedimentation represented by downward advection of the solid and solute. Molecular diffusion for porewater solutes is a
25 function of temperature and salinity and has been calculated with the R package *marelac* (Soetaert et al., 2016) and corrected for tortuosity, following equation 3, deriving the effective diffusion coefficient (Boudreau and Meysman, 2006).

$$D_i = \frac{D_0}{(1 - 2\ln\varphi)} \tag{3}$$

Porosity (φ) is used to obtain the liquid and solid volume fraction in the respective mass balances. The model also includes a set of reactions, where reaction rates (R_k) determine the consumption or production of a species ($\nu_{i,k}$) according to the stoi-

chiometry of the reaction of the ith species in the kth reaction. The reaction set includes 3 primary redox reactions describing the physiological action of microbial degradation of organic matter linked to electron acceptor availability (Table 2). Anaerobic oxidation of methane (AOM) uses CH_4 as electron donor instead of an organic substrate (Boetius et al., 2000). To balance S-species production and consumption, canonical sulphur oxidation is introduced to the reaction set. The kinetic rate expressions

5   are given as second-order rate laws for primary and secondary redox reactions (Table 2; Boudreau, 1997). A sequential electron acceptor usage based on free energy gain of the physiological reactions is ensured by introducing limitation–inhibition formulations (Soetaert et al., 1996; Meysman et al., 2003). To mimic calcium carbonate recrystallization, following an age depth relationship, dissolution and carbonate production reaction rates, expressed as Eq. 4, have been incorporated in the model with no net carbonate dissolution or precipitation (Fantle and DePaolo, 2006, 2007).

10    $$R_{carb}(t) = \frac{0.4}{f_{auth}} \exp(-\frac{t}{0.876 f_{auth}}) \qquad (4)$$

In contrast to the models of Fantle and DePaolo (2006, 2007) we envision that only a fraction of the whole carbonate rock determines the reactivity towards dissolution and recrystallization. This fraction of 0.2 is considered to be the authigenic carbonate fraction (f_{auth}) of the total rock volume (e.g., Schobben et al., 2016). Specific metabolically produced DIC-δ^{13}C values are assigned for organoclastic microbial sulfate reduction, AOM and organoclastic methanogenesis, see Table 2. These

15   metabolic pathways have been considered to induce calcite nucleation by either changing the surrounding carbonate chemistry or destroying calcification-inhibiting organic mucus (Berner et al., 1970; Visscher et al., 2000; Ries et al., 2008; Heindel et al., 2013; Birgel et al., 2015). Peak activity of these metabolic pathways coincides with the most reactive upper layers of the sediment column, i.e., highly porous and high metastable calcite polymorph content (Irwin et al., 1977; Marshall, 1992), and this is mathematically expressed by Eq. 4.

20   Solute diffusion tracts and sedimentation of the carbon isotopes of DIC and solid-phase carbonate are defined as: ^{13}C and ^{12}C, respectively, and are calculated separately. Metabolically introduced carbon ($v_{metabolism}$) by reaction (R_k) and its respective effect on porewater DIC-carbon isotope composition is formulated by Eqs 5 and 6 for the heavy and light isotope, respectively.

$$v_{metabolism} = R_k \frac{1}{1 + r_k} \qquad (5)$$

25    $$v_{metabolism} = R_k \frac{r_k}{1 + r_k} \qquad (6)$$

We assign a ^{13}C/^{12}C-ratio (r) to the metabolism-specific produced DIC from the organic carbon remineralisation reactions according to the data in Table 2. The mathematical formulation of metabolism-introduced DIC ensures that the isotope composition of ambient porewater DIC is altered, whereas mass-balance in the model C in- and output is maintained.

Table 2. Biogeochemical reaction equations and kinetic rate expressions

Biogeochemical reactions	formulation	$\delta^{13}C_{DIC}$	kinetic rate expression
Primary redox reactions			
Oxic respiration	$CH_2O + O_2 \rightarrow HCO_3^- + H^+$	-25 ‰	$\frac{[O_2]}{[O_2]+K_{O_2}} k_{min}[CH_2O]$
Organoclastic sulfate reduction	$CH_2O + \frac{1}{2}SO_4^{2-} \rightarrow HCO_3^- + \frac{1}{2}HS^- + \frac{1}{2}H^+$	-25 ‰	$\frac{[SO_4^{2-}]}{[SO_4^{2-}]+K_{SO_4^{2-}}} \frac{K_{O_2}}{[O_2]+K_{O_2}} k_{min}[CH_2O]$
Organoclastic methanogenesis	$CH_2O \rightarrow \frac{1}{2}CH_4 + \frac{1}{2}CO_2$	+15 ‰	$\frac{K_{SO_4^{2-}}}{[SO_4^{2-}]+K_{SO_4^{2-}}} \frac{K_{O_2}}{[O_2]+K_{O_2}} k_{min}[CH_2O]$
Secondary redox reactions			
Anaerobic oxidation of methane	$CH_4 + SO_4^{2-} \rightarrow HCO_3^- + HS^- + H_2O$	-45 ‰	$\varphi k_{AOM}[SO_4^{2-}][CH_4] \frac{[SO_4^{2-}]}{[SO_4^{2-}]+K_{SO_4^{2-}}}$
Canonical sulphur oxidation	$HS^- + 2O_2 \rightarrow SO_4^{2-} + H^+$	–	$\varphi k_{CSO}[O_2][HS^-]$
Carbonate precipitation/dissolution			
Production authigenic calcite	$Ca^{2+} + 2HCO_3^- \rightarrow CaCO_3 + CO_2 + H_2O$	$\alpha_{carb-DIC}$	$\frac{K_{O_2}}{[O_2]+K_{O_2}} R_{carb}$
Dissolution calcite	$CaCO_3 + CO_2 + H_2O \rightarrow Ca^{2+} + 2HCO_3^-$	$\alpha_{carb-DIC}$	$\frac{K_{O_2}}{[O_2]+K_{O_2}} R_{carb}$

Metabolism-produced carbon isotope values according to Irwin et al. (1977), except organoclastic methanogenesis-sourced CH_4 subsequently employed by AOM which is a conservative estimate between -65 ‰ and near-quantitative sedimentary OC conversion to CH_4, thereby approaching the parent OC-C isotope composition of -25 ‰.

3.2.2 Numerical solutions and parameters

The model includes nine state variables: organic matter (CH_2O), solid carbonate ($^{13}C_{carb}$ and $^{12}C_{carb}$), DIC ($^{13}C_{DIC}$ and $^{12}C_{DIC}$), dissolved oxygen (O_2), dissolved sulfate (SO_4^{2-}), dissolved methane (CH_4), and dissolved sulfide (HS^-). We numerically solved Eqs 1 and 2 on the open-source programming platform R (R Core Team, 2016) with a finite difference approach by expanding the spatial derivatives of partial differential equations over a sediment grid (Boudreau, 1997). By application of the R package *ReacTran* (Soetaert and Meysman, 2012), a sediment grid of 10 m thick with 2000 layers of identical thicknesses was generated. The finite difference approach transforms the partial differentials into ordinary differentials which are subsequently integrated by a stiff solver routine *vode* (Brown and Hindmarsh, 1989), within the R package *DeSolve* (Soetaert et al., 2010). Boundary conditions were chosen to reflect Permian oceanic conditions based on the current state of research (Sect. 2), and complemented with current knowledge of shallow marine environments. For solutes, the upper boundary conditions were set to concentrations for normal modern bottom water conditions, $0.28\,\mu mol\,cm^{-3}$ O_2, $2.2\,\mu mol\,cm^{-3}$ DIC and zero for the reduced species (CH_4 and HS^-). A lower seawater SO_4^{2-} value of $4\,\mu mol\,cm^{-3}$ (compared to the modern value of $28\,\mu mol\,cm^{-3}$) was chosen, following evidence of a reduced global marine S-reservoir in the latest Permian to Early Triassic (Luo et al., 2010; Song et al., 2014; Schobben et al., 2017). The solid phases entering the model at the top of the sediment stack are set at $730\,\mu mol\,cm^{-2}\,y^{-1}$ for both the OC flux (F_{OC}) and the carbonate flux (F_{carb}) in the baseline model, which are typical average shelf sedimentation values (Müller and Suess, 1979; Reimers and Suess, 1983; Sarmiento and Gruber, 2004). For the baseline-condition, sedimentation rates are fixed at $0.2\,cm\,y^{-1}$ and the $\delta^{13}C$ composition is set at $+5\,‰$ (VPDB),

Table 3. Parameter values for the kinetic constants of the reactive-transport model

Constant	Symbol	Unit	Value	Reference
Organic matter reduction				
Decay constant for organic matter	k_{min}	y^{-1}	0.1	a
Monod constant oxygen consumption	K_{O_2}	$\mu\text{mol}\,\text{cm}^{-3}$	0.001	b
Monod constant sulfate reduction	$K_{SO_4^{2-}}$	$\mu\text{mol}\,\text{cm}^{-3}$	0.9	b
Oxidation reactions				
Kinetic constant AOM	k_{AOM}	$\mu\text{mol}\,\text{cm}^{-3}\,\text{y}^{-1}$	1E4	c
Kinetic constant canonical sulphide oxidation	k_{CSO}	$\mu\text{mol}\,\text{cm}^{-3}\,\text{y}^{-1}$	1E4	b

References; a, (Fossing et al., 2004); b, (Meysman et al., 2015); c, (Contreras et al., 2013)

based on primary carbon isotope values from pristine preserved brachiopod calcite from the Ali Bashi and Meishan sections, as well as sites in northern Italy (Korte et al., 2005; Brand et al., 2012b; Schobben et al., 2014). The relation between the isotope composition of DIC and solid phase carbonate is given by the following thermodynamic relation (Eq. 7), established by Emrich et al. (1970), where we assume temperature (T) to be constant at 25 °C

$$\alpha_{carb-DIC} = 1.85 + 0.035[T(^{\circ}C) - 20] \tag{7}$$

The lower boundary conditions for both solid and solute species were set at a "no gradient" boundary, ensuring that materials are only transported by burial to deeper parts of the sediment column. Kinetic parameters are summarized in Table 3, and are based on published models.

3.2.3 Sensitivity tests

The previously defined parameters provide a baseline model to test the sensitivity towards certain boundary conditions, in bringing forward carbon isotope compositional changes in the porewaters, which are eventually incorporated into solid carbonate. Two pathways of authigenic carbonate addition are considered to be of importance for explaining the observed P–Tr δ^{13}C variability; 1) ongoing recrystallization and dissolution with depth after burial, formulated as Eq. 4, and with both processes operating in equilibrium (Fantle and DePaolo, 2006, 2007), and 2) near-instantaneous precipitation of carbonate crusts at (or close to) the seafloor, by microbial mat communities. The latter mechanism would simulate the seafloor crust formation commonly observed for the P–Tr transition, which is recognized as a time of unusual carbonate sedimentation; e.g., stromatolites, thrombolites and microbially induced cementation (Baud et al., 1997; Woods et al., 1999; Leda et al., 2014). We furthermore assume that cryptic forms of carbonate precipitates, e.g., rock-binding cements (e.g., Richoz et al., 2010) might have escaped detection when selecting carbonate rock for carbon isotope studies. These two pathways are henceforward referred to as equilibrium recrystallization and authigenic seafloor cementation, respectively.

Equilibrium recrystallization is determined by taking the evolved solid-phase δ^{13}C at 10 m sediment depth, where carbon isotope exchange between porewater and solid carbonate reaches equilibrium (see also Fantle and DePaolo, 2006, 2007, for a comparative Sr and Ca isotope equilibrium with depth). Although transient seawater chemistry changes can occur over the time needed to complete carbonate stabilization (i.e., before reaching equilibrium at 10 m depth), we consider the adopted iso-

5 tope value to be a good approximation of a partially recrystallized carbonate rock, as diffusion and the majority of metabolic processes are confined to only a small interval of the sediment column (upper ~1 m of the sediment pile). Authigenic seafloor cementation is regarded to take place in the upper 0.1 m of the sediment column by direct precipitation from porewater DIC, which gives the DIC-carbon isotope signature of the ambient porewater (corrected for the equilibrium isotope fractionation, $\alpha_{carb-DIC}$). The evolved bulk-rock carbon isotope value is then calculated by mass balance of primary and authigenic car-

10 bonate components.

An important parameter inducing changes in the vertical structure of a diagenetic redox-profile, and ultimately carbonate-carbon isotope composition of both forms of authigenic precipitate, is the F_{OC}. By systematically changing this parameter we test the sensitivity of the diagenetic baseline model to the OC sinking flux and the consequential organic matter remineralization trajectories, i.e., the dominant microbial communities involved in local *in situ* C-cycling. Besides the OC flux, we performed

15 sensitivity experiments for sedimentation rate, the concentrations of bottom water oxygen and sulfate, as well as the fraction of authigenic carbonate incorporated in the bulk-rock, under equilibrium recrystallization and authigenic seafloor cementation. For each separate sensitivity experiment we return the changing parameter to the initial value, as defined for the baseline model (Sect. 3.2.2), except for the parameter of interest and the OC flux.

4 Results

4.1 First-order temporal trends

By compiling δ^{13}C$_{carb}$ data and unifying it in a biochronological framework, we can distinguish first-order temporal features of the combined Iranian and the Meishan P–Tr (sub)localities in China (Fig. 1). The subsampling routine prevents modifications by unequal sampling intensity, hence this temporal pattern is unbiased by the sampling strategy applied in individual studies. A gradual decline of -4‰ towards depleted δ^{13}C$_{carb}$ can be discerned, starting from the middle Changhsingian, with minimum

25 values reached in the earliest Triassic (0‰), and a return of +2‰ to more enriched δ^{13}C$_{carb}$ values commencing above the *I. isarcica* zone (unit I). Nonetheless, disparity in regional trends is visible as a double-peaked negative excursion marking the P–Tr transitional beds of Meishan, whereas such a signature is absent in time-equivalent boundary beds deposited at the Iranian sites.

By comparing combined subsampled median trend lines of individual studies (constructed following the same statistical

30 routine, as outlined in Sect. 3.1.3) it is possible to analyse whether the first-order isotope trend is a consistent feature of the analysed stratigraphic sequences. A large portion of the compared individual datasets are marked with a high Pearson's correlation coefficient (Fig. 2). We can conclude that the geochemical signal obtained is reproducible and, as such, observable in rock collected during separate sampling campaigns over several decades. However, the comparative study also suggests that
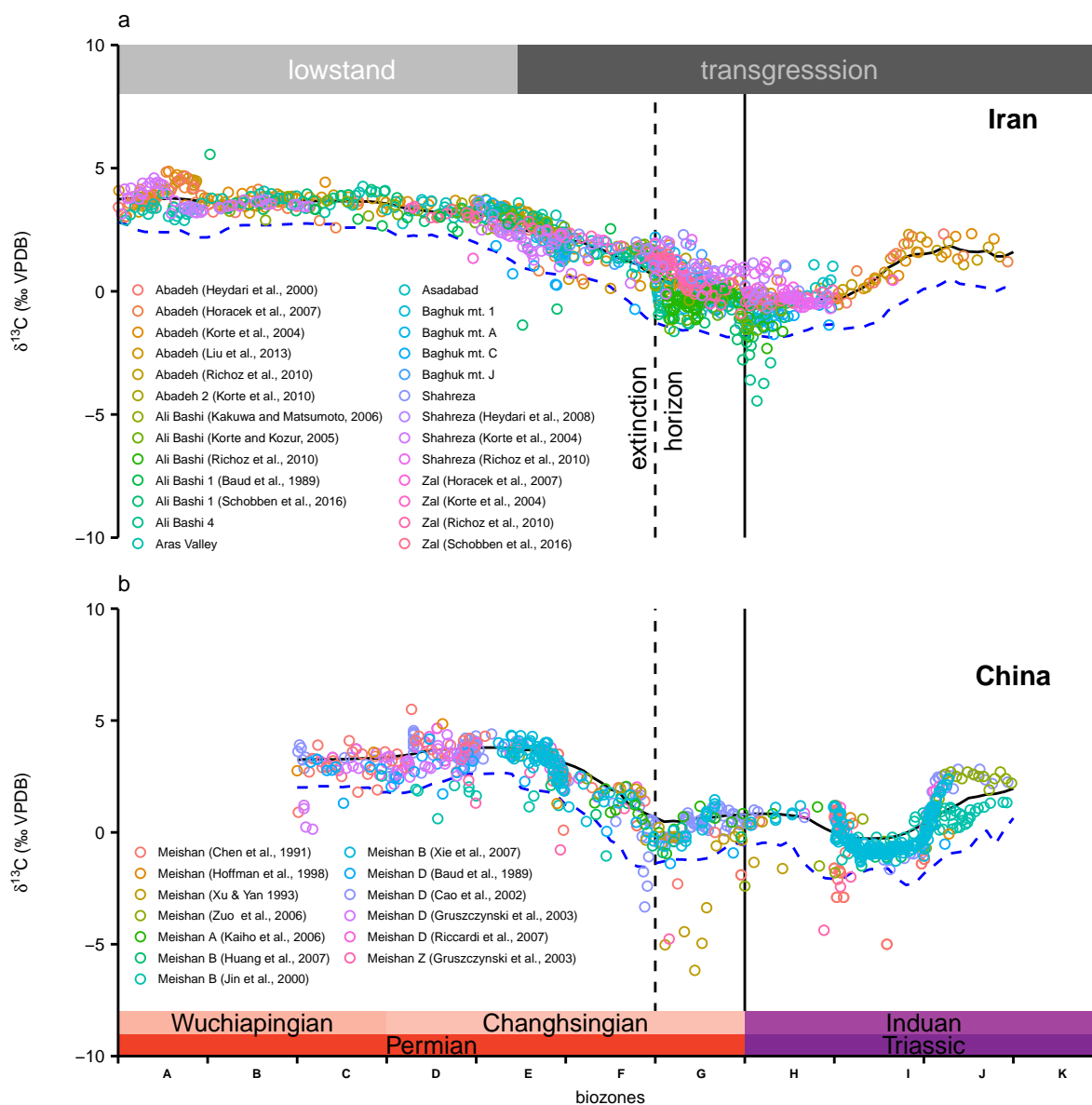
Figure 1. Compiled published and new data for multiple P–Tr rock sequences in Iran (a) and China (b). The individual carbonate carbon isotope values are placed on a dimensionless timeline that marries both geographic areas in the most acceptable biochronological scheme (Table 1). This biostratigraphic scheme furthermore enables the direct comparison of first-order $\delta^{13}C_{carb}$ trends with time-equivalent bio-zones. The solid black line represents the subsampled median trend line. The dashed blue line depicts the seawater $\delta^{13}C_{DIC}$ curve, as obtained from the time series simulation, Sect. 5. The stratigraphic placement of the sea level changes and the extinction horizon as well as the biostratigraphic framework can be found in the Supplementary Information.
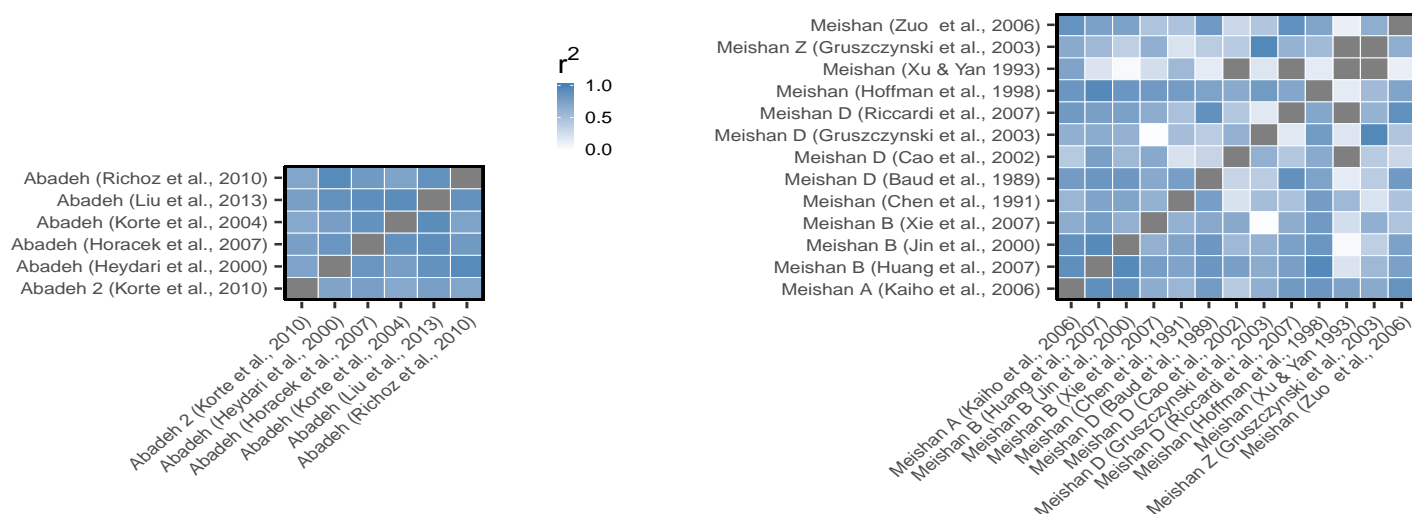
Figure 2. A comparative analysis of first-order temporal trends in $\delta^{13}C_{carb}$ from individual studies for the Abadeh and Meishan (sub)localities. The saturation-level of the individual tiles measures the correlative-strength of stratigraphic trends obtained during individual sampling campaigns, based on the Pearson's correlation coefficient (r^2).

the correlation coefficients are consistently weaker in the Meishan data, relative to the Abadeh data. This lack of reproducibility might stem from limited stratigraphic coverage, e.g. Gruszczyński et al. (2003), which reports on a composite dataset of two sublocalities, Meishan D and Z, and only encompasses Changhsingian strata. Sampling campaigns of reduced stratigraphic coverage might not be able to capture the first-order trend. Nevertheless, region-specific differences in signal reproducibility mark an overall greater disparity between individual Meishan $\delta^{13}C_{carb}$ records, and might point to a higher-order of $\delta^{13}C$ variability.

4.2 Residual carbon isotope variability

Subsampled and time-sliced median interpolations are depicted in Fig. 3. Trends with the highest confidence are highlighted by a well-defined white line, and the width of the CI is represented by a blue colour that becomes less intense with increasing data spread. Combined, these graphing features result in a more blurred image with a larger spread between the median values of individual subsampling routines (Sect. 3.1.3). From these figures we can discern three features in the second-order $\delta^{13}C$ excursions; 1) The residual $\delta^{13}C$ variability is seemingly random or stochastic and defined $\delta^{13}C$ excursions are unreproducible across lithological successions from different geographic locations (Iran), or studies targeting the same site (e.g., Meishan section; Fig. 1). 2) A returning temporal pattern towards decreased fidelity of the median trend line (blurred white trend line) connected with increased CI dispersion (i.e., residual $\delta^{13}C$ variability, seen as less-saturated blue colour-tones), across the extinction horizon and ranging into the Early Triassic, at both geographic locations. Increased maximum $\delta^{13}C$ value-ranges from less than 1 and 2 ‰ (IQR), or 2 and 3 ‰ (IPR) in the pre-extinction beds, to more than 2 and 3 ‰ (IQR) or 5 and 8 ‰ (IPR)

around the extinction horizon, for Iran and China respectively, further enforces the observation of a globally significant peak in residual δ^{13}C variability. This pattern seems to recover after the P–Tr boundary, with generally higher confidence median trend lines and a trend to smaller maximum δ^{13}C value-ranges of less than 2 and 3‰ (IQR), or 5 and 8‰ (IPR) for Iran and China, respectively. 3) In addition, a significant regional offset can be discerned in δ^{13}C value-ranges, where the Chinese profile displays systematically higher residual δ^{13}C variability.

Studies focussing on boundary events (e.g., the P–Tr transition) tend to channel sampling effort at a focal point around the presumed faunal turnover and horizon of palaeoenvironmental change (Wang et al., 2014). Sampling effort is known to have a profound impact on studies that use fossil data to track animal diversity through time (Alroy et al., 2008; Mayhew et al., 2012). By correcting for sampling effect through subsampling (Sect. 3.1.3), we cancelled out the potential effect of over-representative data accumulation on the temporal trend of stochastic residual δ^{13}C$_{\mathrm{carb}}$ variability. Sampling effort might also have affected fossil collecting, thereby biasing conodont biozonation schemes, which heavily relies on the first appearance datum of certain fossil species (Wang et al., 2014; Brosse et al., 2016). When evaluating the average thickness and duration of our chosen biochronological units there is an apparent decrease in unit thickness, as well as shorter duration when approaching the extinction interval (Fig. 3). A comparison of biozone stratigraphic thickness and duration points to a relationship between higher δ^{13}C$_{\mathrm{carb}}$ dispersion and smaller and shorter duration units (Fig. 3). This inverse relationship suggests that δ^{13}C$_{\mathrm{carb}}$ variability is not controlled by the increased potential sample size and the inherent risk of sampling a more variable isotope signature. Hence, we exclude the applied sampling strategy as a causal factor behind the observed temporal trend of stochastic δ^{13}C$_{\mathrm{carb}}$ variability.

4.3 Model response to organic carbon accumulation

In the above, we have conceptualised a model that links sedimentation of organic material to carbonate carbon isotope alteration. An important variable in this model is the amount of organic carbon that arrives at the sea floor, which controls the redox depth profile and the respective importance of metabolic pathways, as reaction per unit area. Low organic carbon fluxes (500 μmol cm^{-3}y^{-1}) yield aerobic respiration as well as microbial-sulfate reduction as important biochemical reactions (Fig. 4). On the other hand, the importance of this metabolic pathway is reduced under high OC accumulation regimes (> 1000 μmol cm^{-3}y^{-1}), which are signified by intense methane production by organoclastic methanogenesis (Fig. 4). Consequently, the dominant organic carbon remineralization pathway determines the final evolved carbon isotope composition of the equilibrated bulk-rock endmember, e.g., towards depleted δ^{13}C$_{\mathrm{carb}}$ under low OC accumulation, and heavier δ^{13}C$_{\mathrm{carb}}$ under high OC loading of the sea floor (Fig. 4).

By systematically changing F_{OC} we see a defined relationship between bulk-rock C isotope alteration and the predominant mode of organic matter remineralization, e.g., by microbial sulfate reducers, AOM or methanogenesis (Fig. 5). The sensitivity experiments further reveal that sedimentation rate, the fraction of authigenic precipitate incorporation, and bottom water oxygenation have only a limited effect on the difference between the primary carbonate precipitate and the bulk-rock endmember C isotope value (Δ^{13}C$_{\mathrm{primary-bulk}}$). In contrast, marine sulfate levels modulate the total range of observed δ^{13}C (~2–3.5‰)
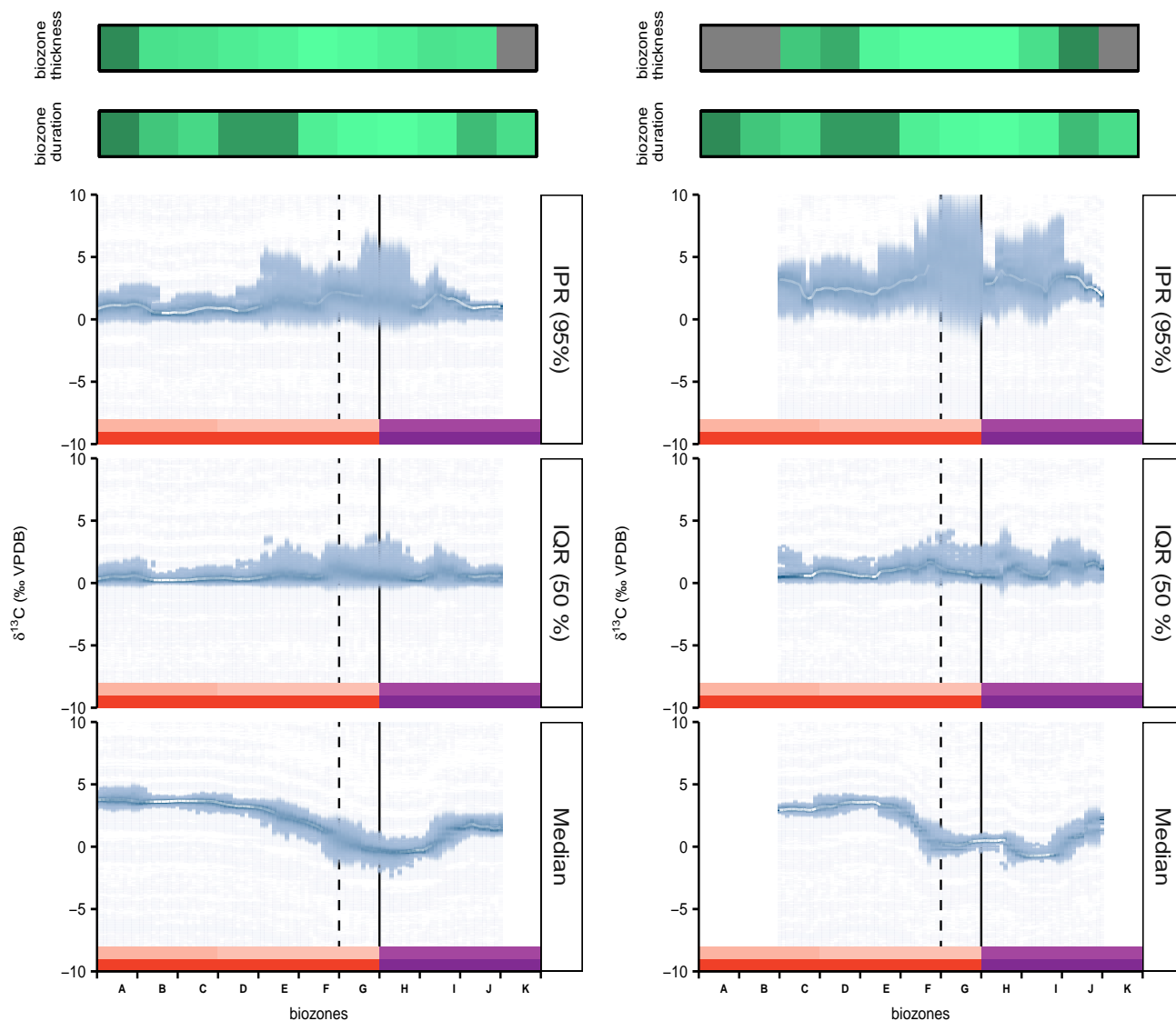
Figure 3. Visually weighted data plot for the Iranian (left) and South China (right) P–Tr (sub)localities (Sect. 3.1.3), depicting the median trend line, the IQR (50 %) and the IPR (95 %) $\delta^{13}C$ value-ranges. Trends with lowest fidelity are marked by a blurring of colours and less contrasted colours (based on the CI of multiple subsample routines). The dashed and the solid line represent the extinction horizon and P–Tr boundary, respectively. The saturation-level of the green tiles in the upper two panels equals the respective biozone thickness and duration. Grey tiles represent intervals with no available biostratigraphic data. See Fig. 1 for colour-legend of the stratigraphic units.

and introduce a switch in the system, which narrows the range of OC accumulation over which the maximum deviation in $\Delta^{13}C_{\mathrm{primary-bulk}}$ occurs (Fig. 5).
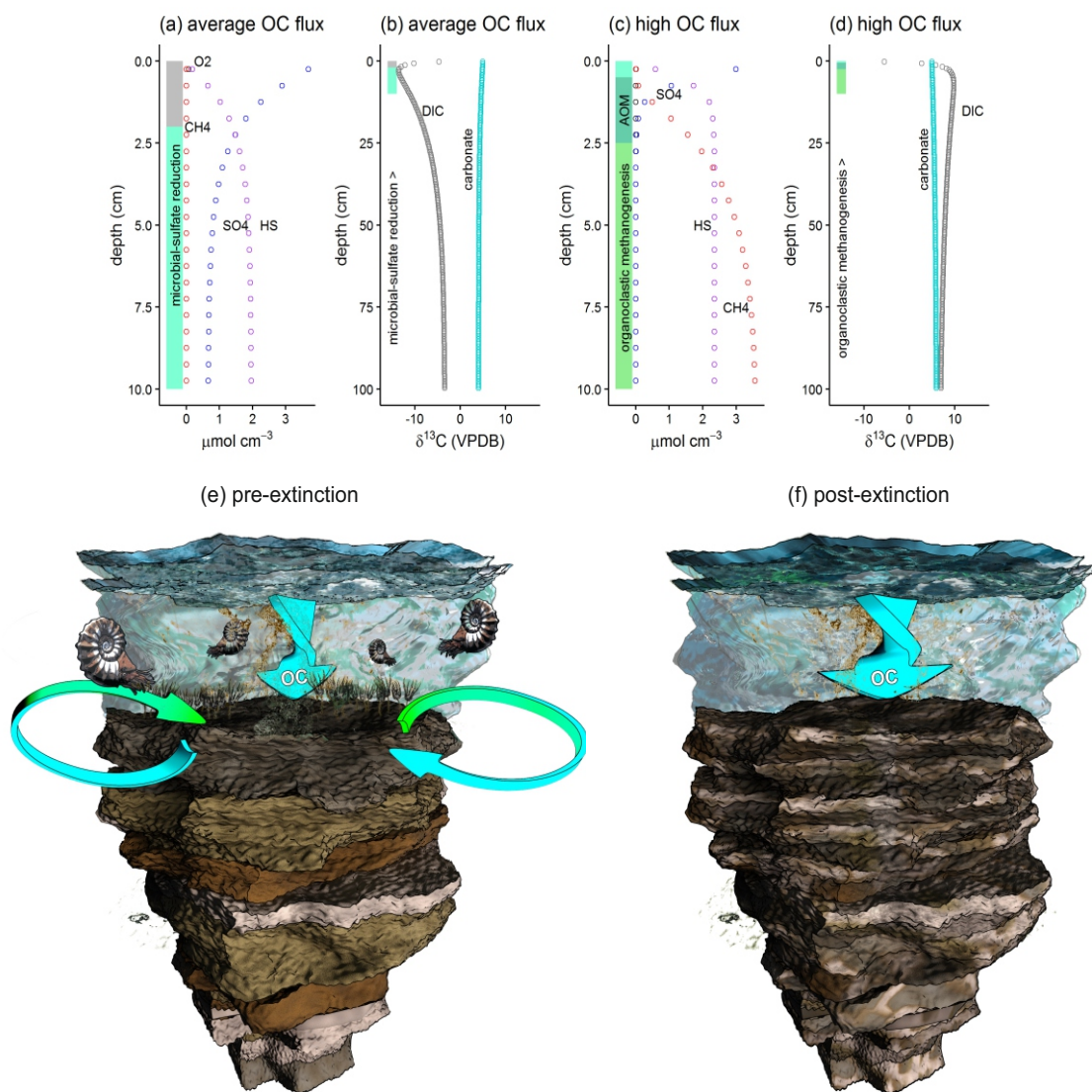
Figure 4. Diagenetic depth profiles of late Permian sea floor sediments of a) oxidized and reduced solutes under an average shelf OC flux $500\,\mu\mathrm{mol\,cm^{-3}y^{-1}}$, b) DIC and authigenic carbonate $\delta^{13}\mathrm{C}$ forced with an average shelf OC flux $500\,\mu\mathrm{mol\,cm^{-3}y^{-1}}$, b) oxidized and reduced solutes under a high OC flux $1200\,\mu\mathrm{mol\,cm^{-3}y^{-1}}$, d) DIC and authigenic carbonate $\delta^{13}\mathrm{C}$ forced with a high OC flux $7000\,\mu\mathrm{mol\,cm^{-3}y^{-1}}$, e) situational sketch of pre-extinction bulk-carbonate accumulation with a normal OC flux and active benthic fauna and f) situational sketch of the post-extinction sedimentation with elevated OC accumulation, removal of metazoan benthic fauna and consequentially reduced sediment mixing (artwork by Mark Schobben).
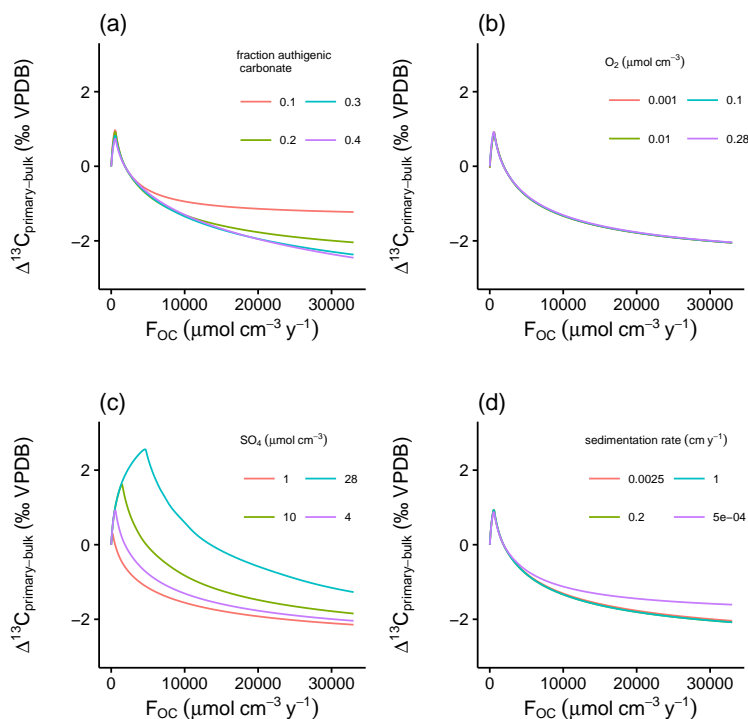
Figure 5. Sensitivity experiment for carbonate rock stabilization by equilibrium recrystallization with depth, designed to investigate the forcing effect of (a) the fraction of authigenic carbonate incorporated, (b) oxygen content of overlying water, (c) sulfate content of overlying water and (d) sedimentation rate, on the carbon isotope offset between the diagenetic endmember rock and the primary calcite, over a range of F_{OC}.

A similar systematic study of OC accumulation results in comparable trajectories of diagenetic C isotope overprinting on bulk-rock (Fig. 6). However, authigenic seafloor cementation results in a 10 ‰-range of attainable bulk-rock endmember C isotope values, which is a wider range than obtained for equilibrium recrystallization. This style of carbonate cementation is also strongly controlled by seawater sulfate concentration. Lower than modern marine dissolved sulfate values ($28\,\mu\mathrm{mol\,cm^{-3}}$) allow for a large range of $\delta^{13}C$ endmember values to be generated under a smaller range of F_{OC} (Fig. 6).

5   Simulation of a virtual carbon isotope time series

In order to understand the obtained temporal patterns in residual $\delta^{13}C_{carb}$ variability, a series of reactive-transport models have been solved to steady state, under varying OC-sedimentation regimes. The virtual time series approach is an amalgamation of multiple sets of individual reactive-transport model runs (100 model iterations = 1 set = 1 time unit), sliding across a timeline of length 100, and with time increments of length one (Fig. 7). The initial organic carbon flux (*the carbon source*; Sect. 2) for the time series simulation was calculated based on the relationship as obtained by the F_{OC} sensitivity experiment with
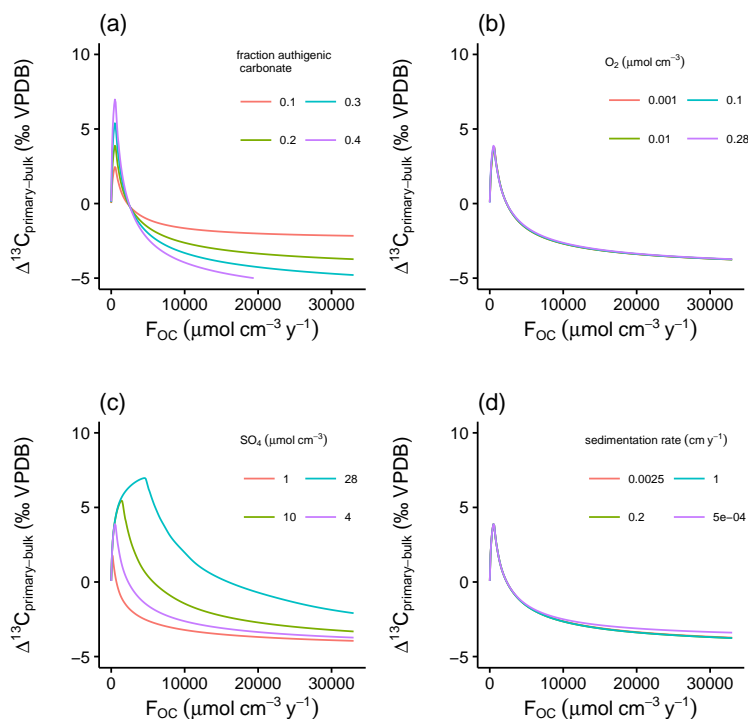
Figure 6. Sensitivity experiment for authigenic seafloor cementation, designed to investigate the forcing effect of (a) the fraction of authigenic carbonate incorporated, (b) oxygen content of overlying water, (c) sulfate content of overlying water and (d) sedimentation rate, on the carbon isotope offset between the diagenetic endmember rock and the primary calcite, over a range of F_{OC}.

baseline conditions (Fig. 5) and the $\Delta^{13}C_{\mathrm{primary-bulk}}$, as obtained from Schobben et al. (2016). The F_{OC} is subsequently modulated for each set (i.e., time unit) based on the observation that OC accumulation increases by a factor of four across the P–Tr transition (Algeo et al., 2013), and by linearly scaling this parameter to the observed residual $\delta^{13}C_{\mathrm{carb}}$ variability (IQR), as obtained from Fig. 3, yielding a continuous range for F_{OC} ($502 \leq F_{OC} \leq 2007\,\mu\mathrm{mol\,cm^{-3}\,y^{-1}}$).

5   With regard to examining the effects of spatially distinct OC sinking fluxes and/or benthic fauna on the lateral distribution of OC (*sediment OC homogeneity*; Sect. 2), we forced individual model runs (within one time unit) with slightly deviating F_{OC} values. The maximum attained F_{OC} variability is constrained by adopting a log-normal skewed density distribution (R package *emdbook*; Bolker, 2008, 2016) around the former established F_{OC}, which represents the population's median value (Fig. 7), and by randomly selecting a value from the created distribution. A log-normal skewed density distribution has been chosen to

10   represent natural variation in the F_{OC}-population, which would be signified by variation that is skewed towards heavy sea floor OC loading in rare instances, whereas most variation is smaller in magnitude and can modulate the flux towards both smaller and higher contributions. Temporal variations in this parameter are attained by modulating the width of the sample population, ranging up to a factor of 1.5. This lateral OC-dispersion parameter is as well linearly scaled to the to the observed residual
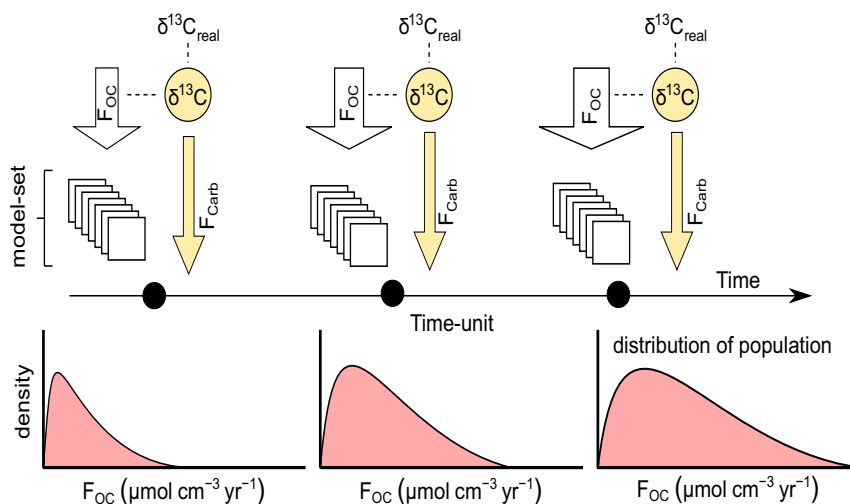
Figure 7. Schematic depiction of the work flow behind the virtual carbon isotope time series. Model sets consist of 100 separate reactive transport model solutions driven by a randomly selected F_{OC} . The randomly generated organic OC-flux values translate into a density distribution with a right skewed tail. Increased F_{OC} and a widening of the value-range is used to simulate increased spatial OC heterogeneity. The carbon isotope value of F_{carb} is obtained from the "real" $\delta^{13}C$ and the relation of $\Delta^{13}C_{\mathrm{primary-bulk}}$ with F_{OC}, as obtained from the sensitivity experiments.

$\delta^{13}C_{\mathrm{carb}}$ variability (IQR), as obtained from Fig. 3. This results in sample-population variations of $328 \leq$ median absolute deviation $\leq 2434 \, \mu\mathrm{mol\,cm^{-3}\,y^{-1}}$, when combined with the initial F_{OC}-range, for homogeneous and more heterogeneous dispersed sedimentary OC, respectively.

The initial carbon isotope composition of F_{carb} is based on the median $\delta^{13}C_{\mathrm{carb}}$ values of the pooled Iranian dataset (Fig. 1)
5 and the $\Delta^{13}C_{\mathrm{primary-bulk}}$, as obtained from Schobben et al. (2016). Subsequent temporal evolution is calculated according to the relationship between the median F_{OC} and $\Delta^{13}C_{\mathrm{primary-bulk}}$, as obtained from Fig. 5, yielding the primary $\delta^{13}C$ of calcium carbonate particles arriving at the seabed for successive time units.

The processes governing increased authigenic seafloor cementation in post-extinction strata are largely speculative. However, undisturbed substrates are a feature required to enable growth of calcifying microbial mats, regardless of the mechanism
10 inducing the global-scale proliferation of these seafloor precipitates (e.g., Garcia-Pichel et al., 2004). Considering this universal control, it is justified to assume a direct link between bioturbation intensity and authigenic seafloor cementation. This assumption links both forms of authigenic carbonate addition: equilibrium recrystallization and authigenic seafloor cementation. The probability (p) of producing authigenic seafloor cements has been assumed to vary linearly between: $0.01 \leq p \leq 0.1$, following the upper two tercile of the range attained by the previous defined OC-dispersion parameter. This definition determines the
15 response of introducing authigenic seafloor cement $\delta^{13}C$ to the sample pool. The f_{auth} for both trajectories of carbonate rock
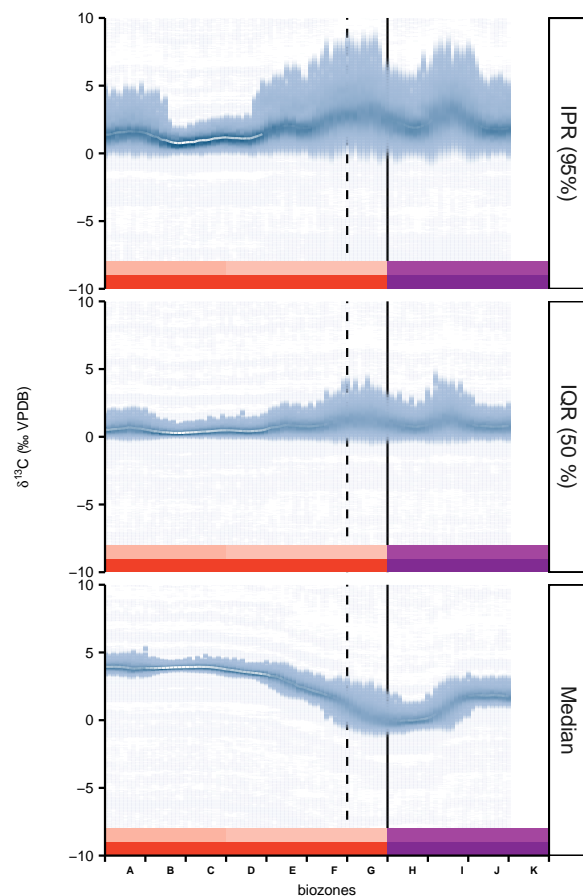
Figure 8. Subsampled virtual carbon isotope time series with model results plotted as "visually weighted" trends. Each time-unit incorporates 100 model iterations with a randomly chosen OC flux from a log-normal skewed density distribution. The time series simulates an increase of four times the average OC flux, an 1.5 times increase in the spatial-heterogeneity of OC accumulation, and increased likelihood of producing seafloor authigenic carbonate to a maximum of 1 in 10.

diagenetic alteration is kept constant at 0.2 (*the diagenetic C isotope recorder*; Sect. 2). The final bulk-rock carbon isotope value is obtained by mass balance from the calculated primary and authigenic carbonate components.

A total of 10,100 reactive-transport models have been solved in order to match the length and resolution of the cumulative "real" δ^{13}C time sequence from sites in Iran (Fig. 1). The resulting virtual time series of model runs forced by previously established value-ranges for the OC sinking flux, sediment homogeneity and authigenic mineral addition is depicted in Fig. 8. By comparing the real and modelled time series, we conclude that the conceptualised model (Sect. 2) and selected parameter values can explain trends in residual carbon isotope variability.

6 Discussion

6.1 Stochastic carbon isotope signatures of the Permian–Triassic boundary beds

Global comparisons of P–Tr carbon isotope records have uncovered disparate δ^{13}C trends and excursions (Fig. 1). These deviations are often encountered on refined stratigraphic and lateral-scales, complicating interregional high-resolution correlations (Heydari et al., 2001; Hermann et al., 2010). Subaerial exposure and projected trajectories of bulk-carbonate stabilization under the influence of meteoric fluids and high water–rock ratios might be invoked to explain this disparity (Heydari et al., 2001; Li and Jones, 2017). Other studies have pointed to stratigraphic variations in predominant mineral rock composition as a source of δ^{13}C$_{carb}$ modulations, citing the mineral-specific isotope offset between aragonite, dolomite and low-Mg calcite (Brand et al., 2012b; Heydari et al., 2013; Schobben et al., 2016; Li and Jones, 2017).

In this study, we provide an alternative explanation for disparate second-order δ^{13}C$_{carb}$ excursions, involving the observed stochastic residual δ^{13}C variability at a refined spatial scale (Fig. 1). We regard this test to be of importance, as a transgression marks the boundary beds and Lower Triassic deposits (Fig. 1). Furthermore, subaerial exposure and consequential early rock stabilization of the studied localities is unlikely to have left an isotopic overprint (Leda et al., 2014; Yin et al., 2014). Also, systematic ^{12}C-depleted bulk-rock relative to brachiopod calcite at the Ali Bashi section (NW Iran), counters the notion of a predominant aragonite precursor for carbonate-rock deposited during the P–Tr transition (Brand et al., 2012b; Heydari et al., 2013). Nonetheless, secondary calcite and dolomite additions might be a causal factor behind observed δ^{13}C variability. However, these additions can also be the result of *in situ* microbially steered mineral formation, which incorporates metabolically produced DIC isotope signatures (Bontognali et al., 2014; Li and Jones, 2017). As such, our conceptualized model is not mutually exclusive with regards to carbonate polymorph compositional changes, but it does not require rapid global secular marine ion inventory changes. Moreover, our model outcome predicts δ^{13}C variation driven solely by small ($f_{auth} = 0.2$) biologically steered mineral contributions (Fig. 6), whereas the recorded δ^{13}C fluctuations are up to 10 times higher in amplitude than otherwise predicted for thermodynamically driven mineral-specific isotope compositional offsets (cf. Brand et al., 2012b; Heydari et al., 2013). Note also, that the mineral-specific isotope offset would require bulk-rock samples to display effectively complete (100 %) mineral compositional changes to a pure carbonate-polymorph composition. In contrast, our model predicts a mechanism that can introduce temporal variation in spatially heterogeneous carbonate polymorph assemblies and associated isotope compositional differences by post-depositional processes, driven by spatially and temporally variable OC accumulation comparable to modern ranges (cf. Müller and Suess, 1979). Depleted marine dissolved sulfate concentrations would have exacerbated the sensitivity of carbonate rock towards only small deviations of this allochthonous C-source (Figs 5 and 6). Combined with a less well-mixed sediment and microbially steered cementation this model can account for the entirety of the observed residual δ^{13}C$_{carb}$ variability.

6.2 Perspectives on the Permian–Triassic carbonate archive: the global biogeochemical carbon cycle, stratigraphy and biological evolution

The first-order P–Tr negative carbon isotope trend can be explained by changes in the sources and sinks of the long-term (> 100 ky) carbon cycle, e.g., a reorganisation of organic carbon burial and volcanic CO_2-outgassing (Renne et al., 1995; Kump and Arthur, 1999; Berner, 2002). Carbon-cycle partitioning between the deep and shallow ocean through the marine biological pump have been proposed to explain the depth-gradient isotope differences (Meyer et al., 2011; Song et al., 2013) or a rapid (< 100 ky) C isotope excursion (Rampino and Caldeira, 2005). On the one hand, the stochastic residual $\delta^{13}C_{carb}$ variability, at confined cm–m stratigraphic-scale, is inherently difficult to reconcile with transient perturbations of the dynamic C-cycle equilibrium enforced by repeated biological reordering of DIC between the shallow and deep ocean (i.e., consecutive events of global productivity increase and wholesale collapse). On the other hand, if lateral variations in marine DIC-C isotope composition accounts for $\delta^{13}C_{carb}$ variability, water column mixing would likely erase spatial compositional differences on smaller scales (< km-scale). For example, residual $\delta^{13}C_{carb}$ variability recorded at Meishan (Fig. 1), at a cm to m-scale, cannot be reconciled with heterogeneity of the overlying watermass, and less well-mixed sediments becomes a more acceptable alternative.

Seafloor methane clathrate dissociation, coal and organic-rich sediment combustion by igneous intrusions as well as ocean Ni-fertilization stimulating methane production by methanogens, are viable sources of transient (< 100 ky) isotope depleted carbon contributions to the atmosphere–ocean system (Erwin, 1993; Knoll et al., 1996; Krull and Retallack, 2000; Retallack and Jahren, 2008; Svensen et al., 2009; Rothman et al., 2014). Although all of the cited mechanisms are conceivable triggers for defined second-order $\delta^{13}C_{carb}$ excursions, they are less likely to create spatially divergent isotope trends and repeated temporally distinct fluctuations, and instead essentially reflect bed-to-bed variation. The existence of transient carbonate isotope excursions is also unlikely, considering the predicted elevated DIC levels of an ocean without pelagic calcifiers, resulting in a conservative behaviour of the DIC-pool towards transient C isotope perturbations (i.e., increasing the systems response time; Kump and Arthur, 1999; Zeebe and Westbroek, 2003; Rampino and Caldeira, 2005). Nonetheless, second-order (transient and depth-gradient) C isotope signals of a primary origin might still be imprinted in the isotope records. However, rock formed under the previously outlined marine depositional conditions (with intensified spatially heterogeneous trajectories of C isotope alteration), increases the chance of sampling spatially variable and diagenetically modulated $\delta^{13}C$ signals, and these would obscure primary signals.

These findings put renewed constraints on the application of whole-rock $\delta^{13}C$ as a high-resolution stratigraphic tool. Diagenesis forced by a recrystallization process, under the influence of meteoric fluids, high fluid to rock ratios, and oxidized terrestrial-derived organics, is generally considered to be the main driver of bulk-rock C isotope alteration (Brand and Veizer, 1981; Marshall, 1992; Brand et al., 2012a, b). Rocks without petrological evidence diagnostic of meteoric fluids percolating through voids and interacting with sediment grains, e.g., paleokarsts, blocky calcite and pendant cements, are usually regarded as pristine and minimally isotopically altered (Veizer et al.; Flügel, 2010; Brand et al., 2012a, b). Regarding the observed P–Tr residual whole-rock $\delta^{13}C$ variability and model predictions, we have shown that under certain marine and sedimentary

situations marine carbonate rock diagenesis can introduce significant δ^{13}C fluctuations to the whole-rock isotope composition. The insight gained here undermines the idea of using second-order δ^{13}C fluctuations as stratigraphic markers, which are often confined to limited stratigraphic intervals (e.g., individual limestone beds), without a proper understanding of the potential effects of diagenetic carbon isotope modification. At least for the data presented here, we can demonstrate that shifts in bulk-rock

5   δ^{13}C smaller than classical biozonation schemes have to be considered with caution, when they coincide with sedimentological features of reduced bioturbation (e.g., lamination), and likely do not serve as a globally universal marker. Instead, long-term first-order trends, cross-cutting formational boundaries (Supplementary Information), have a higher likelihood of representing secular variation in seawater DIC isotope composition, and are largely unaffected by marine diagenetic processes (Fig 1). Extrapolation of our model results to Mesozoic and Cenozoic bulk-carbonate records signified by comparatively reduced δ^{13}C

10   variability might reflect buffering of highly variable diagenetic C isotope contributions under elevated marine sulfate levels and physical sediment mixing by benthic fauna.

     The carbonate chemical signal towards increased δ^{13}C variability supports the global significance of three parameters during deposition of P–Tr carbonate rock: reduced sediment mixing, authigenic precipitates and heterogeneous OC accumulation. Although we have postulated a connection between sediment lamination and C isotope variability, the relation of these obser-

15   vations to the end-Permian mass extinction is unconstrained. The cataclysmic mechanism that drove the extinction of benthic faunas is still a matter of debate, but bottom water anoxia is one of the main contenders. This could have been caused by decreased seawater oxygenation instigated by stagnating ocean circulation (Wignall and Twitchett, 1996; Winguth et al., 2015). Alternatively, a higher OC sinking flux might have led to increased O_2 drawdown by aerobic respiration and H_2S production by sulfate-reducing microbes, leading to widespread marine euxinia (Meyer et al., 2008; Algeo et al., 2013; Schobben et al., 2015).

20   However, δ^{13}C variability complies most compellingly with at least continuing OC accumulation over the studied interval, and thereby largely undermines scenarios of reduced primary productivity (e.g., Rampino and Caldeira, 2005). On the other hand, the proliferation of post-extinction authigenic seafloor precipitates (e.g., thrombolites, stromatolites and fan-shaped structures) likely represents a symptom of reduced sediment disturbance and elevated carbonate saturation (cf. Kershaw et al., 2009). Since some of the more conspicuous post-extinction seafloor structures have been connected with microbial communities and

25   distinct metabolism-mediated isotope signatures (e.g., Heindel et al., 2013), they might be equally important constituents of the observed spatial δ^{13}C variability. Geographic differences observed as systematically higher residual δ^{13}C variability at the Chinese localities are suggestive of a regionally distinct hydrographic and depositional setting. This regional feature could be linked with evidence of episodic Late Permian euxinic conditions in the South China basin (Grice et al., 2005; Cao et al., 2009). Comparatively higher, and spatially variable, OC loading of the sea floor in the South China basin under these circumstances,

30   might be triggered by enhanced primary productivity or OC sinking fluxes (Algeo et al., 2011, 2013). On the other hand, the depositional sites found in Iran lack evidence for bottom water anoxia and favour other drivers behind the marine faunal extinction, e.g. thermal stress or ocean acidification (Leda et al., 2014; Schobben et al., 2014; Clarkson et al., 2015).

     Besides capturing regional biological expressions of the global faunal disruption, our approach illuminates potentially important feedbacks of the Earth system that control the global-scale carbon cycle. Recently, attention has increased on the potential

35   significance of authigenic carbonate production on the global carbonate reservoir, and the addition of authigenic carbon to

Permian and Triassic carbonate-bearing sequences in particular (Schrag et al., 2013; Schobben et al., 2016; Zhao et al., 2016). The numerical exercise highlights the link between local sedimentary OC cycling and bulk-rock diagenetic stabilization, hinting at the potentially significant portion of remineralized OC sequestered by authigenic carbonates. Additionally, bulk-rock residual δ^{13}C variability might serve as an indicator of infaunal biological activity, effectively preserving an ecological signal,

5   which could, in turn, be an indicator of local sedimentary C-cycling. This sub-cycle is strongly controlled by bioturbation and controls the amount of buried organic matter as well as the supply of electron acceptors (Canfield, 1989; Canfield et al., 1993). These fluxes drive carbon removal from the exogenic carbon reservoir and potentially require a revision of generally accepted constraints on these budgets, including during events with postulated major C-cycle perturbations, such as the latest Permian extinction.

10   ## 7   Conclusions

The $\delta^{13}C_{carb}$ record straddling the P–Tr boundary of Iran and South China can be decomposed in a first-order temporal trend, with a negative trend marking the transition beds, and superimposed second-order residual δ^{13}C variability. The primary goal of the current study was to delineate the nature of the second-order δ^{13}C fluctuations, which harbour a reproducible temporal pattern towards increased variability across the extinction beds. By investigating the origin of these second-order geochemical

15   signals it is possible to better constrain the limits of carbon isotope chemostratigraphy, most notably the time resolution on which it can be applied. Having established the fidelity of this signal we discerned that mineralogical heterogeneity as well as meteoric-steered cementation are unsatisfactory candidates to explain the spread in δ^{13}C. Hence, the possibility of metabolism-steered carbonate addition is more likely, noting that the anaerobic microbial pathway introduces isotopically depleted carbon to the porewater, and that the same microbes are often connected with production of authigenic carbonates. Moreover, organic

20   carbon degradation occurs in a part of the sediment column signified by a high reactivity of the primary carbonate sediments. By testing these assumptions with reactive-transport models, and with the construction of a virtual time series, we can recreate the observed variability in the endmember bulk-rock δ^{13}C composition by inducing heterogeneous spatial-distribution of sedimentary OC, i.e., a reduction of physical sediment mixing or spatially divergent OC sinking fluxes. Authigenic seafloor cementation, possibly mediated by microbial mat communities, is another source that might have introduced diagenetic overprints

25   in the P–Tr boundary beds. On the other hand, these mechanisms can still preserve long-term trends of oceanic DIC-carbon isotope composition. These findings strengthen the notion that bulk-carbonate δ^{13}C is a fruitful source of information, recording secular trends in carbon cycle evolution as well as potentially informing us about the biosphere, notably infaunal animal activity, seafloor microbial communities and OC delivery to the seafloor.

8   Code availability

30   Data visualization, statistical data treatment as well as the reactive-transport model have been written in the R-language. The R-scripts are made available on the GitHub repository: https://github.com/MartinSchobben/carbonate (http://doi.org/10.5281/

zenodo.496086).

9   Data availability

The combined data-mined and newly produced $\delta^{13}C$ are made available on the GitHub repository: https://github.com/MartinSchobben/
5   carbonate (http://doi.org/10.5281/zenodo.496086).

Author contributions.   MS designed the study. MS, CK, VH, AG, LL collected material in the field and prepared samples for isotope analysis. US, CK and CVU performed C isotope analysis. MS and SvdV constructed the numerical model. MS and JS data-mined complementary published C isotope results. All authors provided intellectual input and contributed to writing the manuscript.

10   *Competing interests.*   The authors declare that they have no conflict of interest.

Acknowledgements.   We thank Sylvain Richoz (University of Graz, Austria) and Yoshitaka Kakuwa (University of Tokyo, Japan) for providing us with formattable tables of published carbon isotope data. We acknowledge support provided by Aras Free Zone Office and Adel Najafzadeh (Tabriz) to sample the Ali Bashi, Aras Valley and Zal sites, and Bo Petersen (Copenhagen) for analytical assistance in the laboratory. This project was funded by Deutsche Forschungsgemeinschaft (DFG; projects KO1829/12-1, KO1829/12-2 and KO2011/8-1). MS is
15   currently funded by a DFG Research Fellowship (SCHO 1689/1-1), SVDV is supported by a Ph.D. fellowship from the Research Foundation Flanders, CVU acknowledges funding from NERC grant NE/N018508/1, and SWP acknowledges support from a Royal Society Wolfson Research Merit Award.

References

Algeo, T. J., Kuwahara, K., Sano, H., Bates, S., Lyons, T., Elswick, E., Hinnov, L., Ellwood, B., Moser, J., and Maynard, J. B.: Spatial variation in sediment fluxes, redox conditions, and productivity in the Permian-Triassic Panthalassic Ocean, Palaeogeography, Palaeoclimatology, Palaeoecology, 308, 65–83, doi:10.1016/j.palaeo.2010.07.007, http://linkinghub.elsevier.com/retrieve/pii/S0031018210003913, 2011.

Algeo, T. J., Henderson, C. M., Tong, J., Feng, Q., Yin, H., and Tyson, R. V.: Plankton and productivity during the Permian–Triassic boundary crisis: An analysis of organic carbon fluxes, Global and Planetary Change, 105, 52–67, doi:10.1016/j.gloplacha.2012.02.008, http://linkinghub.elsevier.com/retrieve/pii/S0921818112000380, 2013.

Alroy, J., Aberhan, M., Bottjer, D. J., Foote, M., Fürsich, F. T., Harries, P. J., Hendy, A. J. W., Holland, S. M., Ivany, L. C., Kiessling, W., Kosnik, M. a., Marshall, C. R., McGowan, A. J., Miller, A. I., Olszewski, T. D., Patzkowsky, M. E., Peters, S. E., Villier, L., Wagner, P. J., Bonuso, N., Borkow, P. S., Brenneis, B., Clapham, M. E., Fall, L. M., Ferguson, C. a., Hanson, V. L., Krug, A. Z., Layou, K. M., Leckey, E. H., Nürnberg, S., Powers, C. M., Sessa, J. a., Simpson, C., Tomasovych, A., and Visaggi, C. C.: Phanerozoic trends in the global diversity of marine invertebrates, Science, 321, 97–100, doi:10.1126/science.1156963, http://science.sciencemag.org/content/321/5885/97, 2008.

Auguie, B.: gridExtra: Miscellaneous Functions for "Grid" Graphics, http://CRAN.R-project.org/package=gridExtra, r package version 2.0.0, 2016.

Banner, J. L. and Hanson, G. N.: Calculation of simultaneous isotopic and trace element variations during water-rock interaction with applications to carbonate diagenesis, Geochimica et Cosmochimica Acta, 54, 3123–3137, doi:10.1016/0016-7037(90)90128-8, http://www.sciencedirect.com/science/article/pii/0016703790901288, 1990.

Bathurst, R. G. C.: Cementation, in: Developments in sedimentology 12: Carbonate sediments annd their diagenesis, chap. 10, pp. 415–457, Elservier, doi:10.1016/S0070-4571(08)70904-X, http://www.sciencedirect.com/science/article/pii/S007045710870904X, 1975.

Baud, A., Magaritz, M., and Holser, W. T.: Permian-Triassic of the Tethys: Carbon isotope studies, Geologische Rundschau, 78, 649–677, 1989.

Baud, A., Cirilli, S., and Marcoux, J.: Biotic response to mas extinction: the lowermost Triasic Microbialites, Facies, 36, 238–242, 1997.

Berner, R. A.: An idealized model of dissolved sulfate distribution in recent sediments, Geochimica et Cosmochimica Acta, 28, 1497–1503, doi:10.1016/0016-7037(64)90164-4, 1964.

Berner, R. A.: Examination of hypotheses for the Permo-Triassic boundary extinction by carbon cycle modeling., Proceedings of the National Academy of Sciences of the United States of America, 99, 4172–4177, doi:10.1073/pnas.032095199, http://www.pnas.org/content/99/7/4172.abstract, 2002.

Berner, R. a., Scott, M. R., and Thomlinson, C.: Carbonate alkalinity in the pore waters of anoxic marine sediments, Limnology and Oceanography, 15, 544–549, doi:10.4319/lo.1970.15.4.0544, http://onlinelibrary.wiley.com/doi/10.4319/lo.1970.15.4.0544/abstract, 1970.

Birgel, D., Meister, P., Lundberg, R., Horath, T. D., Bontognali, T. R. R., Bahniuk, A. M., de Rezende, C. E., Vasconcelos, C., and McKenzie, J. A.: Methanogenesis produces strong ^{13}C enrichment in stromatolites of Lagoa Salgada, Brazil: a modern analogue for Palaeo-/Neoproterozoic stromatolites?, Geobiology, 13, 245–266, doi:10.1111/gbi.12130, http://doi.wiley.com/10.1111/gbi.12130, 2015.

Boetius, A., Ravenschlag, K., Schubert, C. J., Rickert, D., Widdel, F., Gieseke, A., Amann, R., Jørgensen, B. B., Witte, U., and Pfannkuche, O.: A marine microbial consortium apparently mediating anaerobic oxidation of methane, Nature, 407, 623–626, doi:10.1038/35036572, http://www.nature.com/doifinder/10.1038/35036572, 2000.

Bolker, B.: emdbook: Ecological Models and Data in R, https://CRAN.R-project.org/package=emdbook, r package version 1.3.9., 2016.

Bolker, B. M.: Ecological Models and Data in R, Princeton University Press, 2008.

Bontognali, T. R. R., Mckenzie, J. A., Warthmann, R. J., and Vasconcelos, C.: Microbially influenced formation of Mg-calcite and Ca-dolomite in the presence of exopolymeric substances produced by sulphate-reducing bacteria, Terra Nova, 26, 72–77, doi:10.1111/ter.12072, http://onlinelibrary.wiley.com/doi/10.1111/ter.12072/abstract, 2014.

5 Boudreau, B. P.: Diagenetic models and their implementation. Modelling transport and reactions in aquatic sediments, 3, Springer, New York, doi:0.I007/97S-3-642-60421-S, http://dalspace.library.dal.ca/handle/10222/49856, 1997.

Boudreau, B. P. and Meysman, F. J. R.: Predicted tortuosity of muds, Geology, 34, 693–696, doi:10.1130/G22771.1, http://geology.gsapubs.org/content/34/8/693.abstract, 2006.

Brand, U. and Veizer, J.: Chemical diagenesis of a multicomponent carbonate system-1: Trace elements, Journal of Sedi-
10 mentary Research, 50, 1219 –1236, doi:10.1306/212F7BB7-2B24-11D7-8648000102C1865D, http://jsedres.sepmonline.org/content/50/4/1219.abstract{%}5Cnhttp://libsta28.lib.cam.ac.uk:2337/content/50/4/1219.full.pdf{%}5Cnhttp://libsta28.lib.cam.ac.uk:2337/content/50/4/1219.full.pdf+html?frame=sidebar, 1980.

Brand, U. and Veizer, J.: Chemical diagenesis of a multicomponent carbonate system -2: Stable isotopes, Journal of Sedimentary Pertrology, 51, 987–997, doi:10.1306/212F7DF6-2B24-11D7-8648000102C1865D, http://jsedres.geoscienceworld.org/content/51/3/987, 1981.

15 Brand, U., Jiang, G., Azmy, K., Bishop, J., and Montañez, I. P.: Diagenetic evaluation of a Pennsylvanian carbonate succession (Bird Spring Formation, Arrow Canyon, Nevada, U.S.A.) — 1: Brachiopod and whole rock comparison, Chemical Geology, 308-309, 26–39, doi:10.1016/j.chemgeo.2012.03.017, http://linkinghub.elsevier.com/retrieve/pii/S0009254112001428, 2012a.

Brand, U., Posenato, R., Came, R., Affek, H., Angiolini, L., Azmy, K., and Farabegoli, E.: The end-Permian mass extinction: A rapid volcanic CO_2 and CH_4 climatic catastrophe, Chemical Geology, 322, 121–144, doi:10.1016/j.chemgeo.2012.06.015, http://linkinghub.
20 elsevier.com/retrieve/pii/S0009254112002938, 2012b.

Brosse, M., Bucher, H., and Goudemand, N.: Quantitative biochronology of the Permian-Triassic boundary in South China based on conodont unitary associations, Earth-Science Reviews, 155, 153–171, doi:10.1016/j.earscirev.2016.02.003, http://dx.doi.org/10.1016/j.earscirev.2016.02.003, 2016.

Brown, P. N. and Hindmarsh, A. C.: Reduced storage matrix methods in stiff ODE systems, Applied Mathematics and Computation, 31,
25 40–91, doi:10.1016/0096-3003(89)90110-0, http://www.sciencedirect.com/science/article/pii/0096300389901100, 1989.

Busenberg, E. and Plummer, L. N.: Thermodynamics of magnesian calcite solid-solutions at 25°C and 1 atm total pressure, Geochimica et Cosmochimica Acta, 53, 1189–1208, doi:10.1016/0016-7037(89)90056-2, http://www.sciencedirect.com/science/article/pii/0016703789900562, 1989.

Canfield, D. E.: Sulfate reduction and oxic respiration in marine sediments: implications for organic carbon preservation in euxinic en-
30 vironments., Deep- Sea Research, 36, 121–138, doi:10.1016/0198-0149(89)90022-8, http://www.sciencedirect.com/science/article/pii/0198014989900228, 1989.

Canfield, D. E., Jorgensen, B. B., Fossing, H., Glud, R., Gundersen, J., Ramsing, N. B., Thamdrup, B., Hansen, J. W., Nielsen, L. P., and Hall, P. O.: Pathways of organic carbon oxidation in three continental margin sediments., Marine geology, 113, 27–40, doi:10.1016/0025-3227(93)90147-N, http://www.sciencedirect.com/science/article/pii/002532279390147N, 1993.

35 Cao, C., Wang, W., and Jin, Y.: Carbon isotope excursions across the Permian-Triassic boundary in the Meishan section , Zhejiang Province , China, Chinese Science Bulletin, 47, 1125–1129, doi:10.1360/02tb9252, http://link.springer.com/article/10.1360/02tb9252, 2002.

Cao, C., Love, G. D., Hays, L. E., Wang, W., Shen, S., and Summons, R. E.: Biogeochemical evidence for euxinic oceans and ecological disturbance presaging the end-Permian mass extinction event, Earth and Planetary Science Letters, 281, 188–201, doi:10.1016/j.epsl.2009.02.012, http://linkinghub.elsevier.com/retrieve/pii/S0012821X09001083, 2009.

Chen, J.-S., Chu, X.-L., Shao, M.-R., and Zhong, H.: Carbon isotope study of the Permian-Triassic boundary sequences in China, Chemical Geology: Isotope Geoscience Section, 86, 239–251, doi:10.1016/0168-9622(91)90052-X, http://www.sciencedirect.com/science/article/pii/016896229190052X, 1991.

Clarkson, M. O., Kasemann, S. A., Wood, R. A., Lenton, T. M., Daines, S. J., Richoz, S., Ohnemueller, F., Meixner, A., Poulton, S. W., and Tipper, E. T.: Ocean acidification and the Permo-Triassic mass extinction., Science, 348, 229–232, doi:10.1126/science.aaa0193, http://science.sciencemag.org/content/348/6231/229, 2015.

Contreras, S., Meister, P., Liu, B., Prieto-mollar, X., Hinrichs, K.-u., and Khalili, A.: subsea floor redox zonation on the Peruvian shelf, Proceedings of the National Academy of Sciences, 110, 1–6, doi:10.1073/pnas.1305981110/-/DCSupplemental.www.pnas.org/cgi/doi/10.1073/pnas.1305981110, www.pnas.org/cgi/doi/10.1073/pnas.1305981110, 2013.

Dickens, G. R., O'Neil, J. R., Rea, D. K., and Owen, R. M.: Dissociation of oceanic methane hydrate as a cause of the carbon isotope excursion at the end of the Paleocene, Paleoceanography, 10, 965–971, doi:10.1029/95PA02087, http://onlinelibrary.wiley.com/doi/10.1029/95PA02087/abstract, 1995.

Emrich, K., Ehhalt, D. H., and Vogel, J. C.: Carbon isotope fractionation during the precipitation of calcium carbonate, Earth and Planetary Science Letters, 8, 363–371, doi:10.1016/0012-821X(70)90109-3, http://www.sciencedirect.com/science/article/pii/0012821X70901093, 1970.

Erwin, D. H.: The great Paleozoic crisis. Life and Death in the Permian., Columbia University Press, New York, 1993.

Fantle, M. S. and DePaolo, D. J.: Sr isotopes and pore fluid chemistry in carbonate sediment of the Ontong Java Plateau: Calcite recrystallization rates and evidence for a rapid rise in seawater Mg over the last 10 million years, Geochimica et Cosmochimica Acta, 70, 3883–3904, doi:10.1016/j.gca.2006.06.009, http://www.sciencedirect.com/science/article/pii/S0016703706002882, 2006.

Fantle, M. S. and DePaolo, D. J.: Ca isotopes in carbonate sediment and pore fluid from ODP Site 807A: The Ca2+(aq)-calcite equilibrium fractionation factor and calcite recrystallization rates in Pleistocene sediments, Geochimica et Cosmochimica Acta, 71, 2524–2546, doi:10.1016/j.gca.2007.03.006, http://www.sciencedirect.com/science/article/pii/S0016703707001299, 2007.

Flügel, E.: Microfacies of Carbonate Rocks, Springer-Verlag, Berlin Heidelberg, 2 edn., doi:10.1007/978-3-662-08726-8, 2010.

Fossing, H., Berg, P., Thamdrup, B., Rysgaard, S., and Munk, H.: A model set-up for an oxygen and nutrient flux model for Aarhus Bay (Denmark), 483, http://www.2.dmu.dk/1{_}Viden/2{_}Publikationer/3{_}fagrapporter/rapporter/FR483.PDF, 2004.

Froelich, P. N., Klinkhammer, G. P., Bender, M. L., Luedtke, N. A., Heath, G. R., Cullen, D., Dauphin, P., Hammond, D., Hartman, B., and Maynard, V.: Early oxidation of organic matter in pelagic sediments of the eastern equatorial Atlantic: suboxic diagenesis, Geochimica et Cosmochimica Acta, 43, 1075–1090, doi:10.1016/0016-7037(79)90095-4, http://www.sciencedirect.com/science/article/pii/0016703779900954, 1979.

Garcia-Pichel, F., Al-Horani, F. a., Farmer, J. D., Ludwig, R., and Wade, B. D.: Balance between microbial calcification and metazoan bioerosion in modern stromatolitic oncolites, Geobiology, 2, 49–57, doi:10.1111/j.1472-4669.2004.00017.x, http://dx.doi.org/10.1111/j.1472-4669.2004.00017.x, 2004.

Grice, K., Cao, C., Love, G. D., Böttcher, M. E., Twitchett, R. J., Grosjean, E., Summons, R. E., Turgeon, S. C., Dunning, W., and Jin, Y.: Photic zone euxinia during the Permian-Triassic superanoxic event, Science, 307, 706–9, doi:10.1126/science.1104323, http://science.sciencemag.org/content/307/5710/706, 2005.

Gruszczyński, M., Małkowski, K., Szaniawski, H., and Cheng-Yuan, W.: The carbon biogeochemical cycle across the Permian - Triassic boundary strata and its implications: Isotope record from the Changhsingian Stage at Meishan, south China, Acta Geologica Polonica, 53, 167–179, http://www.scopus.com/inward/record.url?eid=2-s2.0-0142228695{&}partnerID=40{&}md5=db2f5d722845c675c6e97e56fae445c5, 2003.

5   Heindel, K., Richoz, S., Birgel, D., Brandner, R., Klügel, A., Krystyn, L., Baud, A., Horacek, M., Mohtat, T., and Peckmann, J.: Biogeochemical formation of calyx-shaped carbonate crystal fans in the subsurface of the Early Triassic seafloor, Gondwana Research, doi:10.1016/j.gr.2013.11.004, http://linkinghub.elsevier.com/retrieve/pii/S1342937X13003675, 2013.

Hermann, E., Hochuli, P. a., Bucher, H., Vigran, J. O., Weissert, H., and Bernasconi, S. M.: A close-up view of the Permian–Triassic boundary based on expanded organic carbon isotope records from Norway (Trøndelag and Finnmark Platform), Global and Planetary Change, 74,
10   156–167, doi:10.1016/j.gloplacha.2010.10.007, http://linkinghub.elsevier.com/retrieve/pii/S0921818110002316, 2010.

Heydari, E., Hassandzadeh, J., and Wade, W. J.: Geochemistry of central tethyan Upper Permian and Lower Triassic strata, Abadeh region, Iran, Sedimentary Geology, 137, 85–99, doi:10.1016/S0037-0738(00)00138-X, http://www.sciencedirect.com/science/article/pii/S003707380000138X, 2000.

Heydari, E., Wade, W. J., and Hassanzadeh, J.: Diagenetic origin of carbon and oxygen isotope compositions of Permian-Triassic boundary strata, Sedimentary Geology, 143, 191–197, doi:10.1016/S0037-0738(01)00095-1, http://www.sciencedirect.com/science/article/pii/S0037073801000951, 2001.

Heydari, E., Arzani, N., and Hassanzadeh, J.: Mantle plume: The invisible serial killer — Application to the Permian–Triassic boundary mass extinction, Palaeogeography, Palaeoclimatology, Palaeoecology, 264, 147–162, doi:10.1016/j.palaeo.2008.04.013, http://linkinghub.elsevier.com/retrieve/pii/S0031018208002150, 2008.

20   Heydari, E., Arzani, N., Safaei, M., and Hassanzadeh, J.: Ocean's response to a changing climate: Clues from variations in carbonate mineralogy across the Permian-Triassic boundary of the Shareza Section, Iran, Global and Planetary Change, 105, 79–90, doi:10.1016/j.gloplacha.2012.12.013, http://linkinghub.elsevier.com/retrieve/pii/S092181811200241X, 2013.

Hoffman, A., Gruszczynskj, M., Malkowskj, K., and Wski, H. S.: Should the Permian/Triassic boundary be defined by the carbon isotope shift?, Acta Geologica Polonica, 48, 141–148, https://geojournals.pgi.gov.pl/agp/article/view/10354, 1998.

25   Hofmann, R., Buatois, L., MacNaughton, R., and Mángano, M.: Loss of the sedimentary mixed layer as a result of the end-Permian extinction, Palaeogeography, Palaeoclimatology, Palaeoecology, 428, 1–11, doi:10.1016/j.palaeo.2015.03.036, http://linkinghub.elsevier.com/retrieve/pii/S0031018215001674, 2015.

Horacek, M., Richoz, S., Brandner, R., Krystyn, L., and Spötl, C.: Evidence for recurrent changes in Lower Triassic oceanic circulation of the Tethys: The δ^{13}C record from marine sections in Iran, Palaeogeography, Palaeoclimatology, Palaeoecology, 252, 355–369,
30   doi:10.1016/j.palaeo.2006.11.052, http://linkinghub.elsevier.com/retrieve/pii/S0031018207001289, 2007.

Hsiang, S. M.: Visually-Weighted Regression, http://www.fight-entropy.com/2012/08/watercolor-regression.html, 2012.

Huang, J., Luo, G., Bai, X., and Tang, X.: Organic fraction of the total carbon burial flux deduced from carbon isotopes across the Permo-Triassic boundary at Meishan, Zhejiang Province, China, Frontiers of Earth Science in China, 1, 425–430, doi:10.1007/s11707-007-0052-z, http://link.springer.com/article/10.1007/s11707-007-0052-z, 2007.

35   Irwin, H., Curtis, C., and Coleman, M.: Isotopic evidence for source of diagenetic carbonates formed during burial of organic-rich sediments, Nature, 269, 209–213, doi:10.1038/269209a0, http://www.nature.com/nature/journal/v269/n5625/abs/269209a0.html, 1977.

Jin, Y., Wang, Y., Wang, W., Shang, Q., Cao, C., and Erwin, D.: Pattern of marine mass extinction near the Permian-Triassic boundary in South China., Science, 289, 432–436, doi:10.1126/science.289.5478.432, http://science.sciencemag.org/content/289/5478/432.full?maxtoshow=

{&}HITS=10{&}hits=10{&}RESULTFORMAT={&}titleabstract=Permian{&}searchid=QID{_}NOT{_}SET{&}stored{_}search=
{&}FIRSTINDEX=0{&}fdate=10/1/1995{&}tdate=7/31/2001, 2000.

Kaiho, K., Kajiwara, Y., Chen, Z.-Q., and Gorjan, P.: A sulfur isotope event at the end of the Permian, Chemical Geology, 235, 33–47,
doi:10.1016/j.chemgeo.2006.06.001, http://linkinghub.elsevier.com/retrieve/pii/S0009254106002786, 2006.

Kakuwa, Y. and Matsumoto, R.: Cerium negative anomaly just before the Permian and Triassic boundary event — The upward expansion
of anoxia in the water column, Palaeogeography, Palaeoclimatology, Palaeoecology, 229, 335–344, doi:10.1016/j.palaeo.2005.07.005,
http://linkinghub.elsevier.com/retrieve/pii/S0031018205004086, 2006.

Kershaw, S., Li, Y., Crasquin-soleau, S., Feng, Q., Mu, X., Collin, P.-y., Reynolds, A., and Guo, L.: Earliest Triassic microbialites in the
South China block and other areas: controls on their growth and distribution, Facies, 53, 409–425, doi:10.1007/s10347-007-0105-5,
http://link.springer.com/10.1007/s10347-007-0105-5, 2007.

Kershaw, S., Crasquin, S., Collin, P.-Y., Li, Y., Feng, Q., and Forel, M.-B.: Microbialites as disaster forms in anachronistic facies following
the end-Permian mass extinction: a discussion, Australian Journal of Earth Sciences, 56, 809–813, doi:10.1080/08120090903002623,
http://www.tandfonline.com/doi/abs/10.1080/08120090903002623, 2009.

Knauth, L. P. and Kennedy, M. J.: The late Precambrian greening of the Earth., Nature, 460, 728–32, doi:10.1038/nature08213, http://www.
nature.com/nature/journal/v460/n7256/full/nature08213.html, 2009.

Knoll, A. H., Bambach, R. K., Canfield, D. E., and Grotzinger, J. P.: Comparative Earth history and Late Permian mass extinction, Science,
273, 452–457, doi:10.1126/science.273.5274.452, http://science.sciencemag.org/content/273/5274/452, 1996.

Knoll, A. H., Bambach, R. K., Payne, J. L., Pruss, S., and Fischer, W. W.: Paleophysiology and end-Permian mass extinction, Earth and Plan-
etary Science Letters, 256, 295–313, doi:10.1016/j.epsl.2007.02.018, http://linkinghub.elsevier.com/retrieve/pii/S0012821X07000842,
2007.

Korte, C. and Kozur, H. W.: Carbon isotope stratigraphy across the Permian/Triassic at Jolfa (NW-Iran, Peitlerkofel (Sas de Pütia, Sass de
Putia, Pufels (Bula, Bulla), Tesero (all three Southern Alps Italy) and Gerennavár (Bükk Mts., Hungary), Journal of Alpine Geology, 47,
119–135, 2005.

Korte, C., Kozur, H., and Mohtat-Aghai, P.: Dzhulfian to lowermost Triassic δ^{13}C record at the Permian/Triassic boundary section at Shahreza
, Central Iran, Hallesches Jahrbuech Geowissenschaften, Reihe B, 18, 73–78, http://www.geo.uni-halle.de/services/publikationen/hjgw/
beihefte/, 2004a.

Korte, C., Kozur, H. W., Joachimski, M. M., Strauss, H., Veizer, J., and Schwark, L.: Carbon, sulfur, oxygen and strontium isotope records,
organic geochemistry and biostratigraphy across the Permian/Triassic boundary in Abadeh, Iran, International Journal of Earth Sciences,
93, 565–581, doi:10.1007/s00531-004-0406-7, http://link.springer.com/10.1007/s00531-004-0406-7, 2004b.

Korte, C., Kozur, H. W., and Partoazar, H.: Negative carbon isotope excursion at the Permian/Triassic boundary section at Zal, NW-Iran,
Hallesches Jahrbuech Geowissenschaften, Reihe B, Beiheft 18, 69–71, http://www.geo.uni-halle.de/services/publikationen/hjgw/beihefte/,
2004c.

Korte, C., Jasper, T., Kozur, H. W., and Veizer, J.: δ^{18}O and δ^{13}C of Permian brachiopods: A record of seawater evolution and continen-
tal glaciation, Palaeogeography, Palaeoclimatology, Palaeoecology, 224, 333–351, doi:10.1016/j.palaeo.2005.03.015, http://linkinghub.
elsevier.com/retrieve/pii/S0031018205001379, 2005.

Korte, C., Pande, P., Kalia, P., Kozur, H. W., Joachimski, M. M., and Oberhänsli, H.: Massive volcanism at the Permian-Triassic
boundary and its impact on the isotopic composition of the ocean and atmosphere, Journal of Asian Earth Sciences, 37, 293–311,
doi:10.1016/j.jseaes.2009.08.012, http://linkinghub.elsevier.com/retrieve/pii/S1367912009002028, 2010.

Krull, E. S. and Retallack, G. J.: δ^{13}C depth profiles from paleosols across the Permian-Triassic boundary: Evidence for methane release, Bulletin of the Geological Society of America, 112, 1459–1472, doi:10.1130/0016-7606(2000)112<1459:CDPFPA>2.0.CO;2, http://gsabulletin.gsapubs.org/content/112/9/1459.short, 2000.

Kump, L. R. and Arthur, M. A.: Interpreting carbon-isotope excursions: carbonates and organic matter, Chemical Geology, 161, 181–198, doi:10.1016/S0009-2541(99)00086-8, http://www.sciencedirect.com/science/article/pii/S0009254199000868, 1999.

Leda, L., Korn, D., Ghaderi, A., Hairapetian, V., Struck, U., and Reimold, W. U.: Lithostratigraphy and carbonate microfacies across the Permian–Triassic boundary near Julfa (NW Iran) and in the Baghuk Mountains (Central Iran), Facies, 60, 295–325, doi:10.1007/s10347-013-0366-0, http://link.springer.com/10.1007/s10347-013-0366-0, 2014.

Li, R. and Jones, B.: Diagenetic overprint on negative δ13C excursions across the Permian/Triassic boundary: A case study from Meishan section, China, Palaeogeography, Palaeoclimatology, Palaeoecology, 468, 18–33, doi:10.1016/j.palaeo.2016.11.044, http://linkinghub.elsevier.com/retrieve/pii/S0031018216307933, 2017.

Liu, X.-c., Wang, W., zhong Shen, S., Gorgij, M. N., cheng Ye, F., chun Zhang, Y., Furuyama, S., Kano, A., and zheng Chen, X.: Late Guadalupian to Lopingian (Permian) carbon and strontium isotopic chemostratigraphy in the Abadeh section, central Iran, Gondwana Research, 24, 222–232, doi:10.1016/j.gr.2012.10.012, http://linkinghub.elsevier.com/retrieve/pii/S1342937X12003498, 2013.

Luo, G., Kump, L. R., Wang, Y., Tong, J., Arthur, M. a., Yang, H., Huang, J., Yin, H., and Xie, S.: Isotopic evidence for an anomalously low oceanic sulfate concentration following end-Permian mass extinction, Earth and Planetary Science Letters, 300, 101–111, doi:10.1016/j.epsl.2010.09.041, http://linkinghub.elsevier.com/retrieve/pii/S0012821X10006163, 2010.

Marshall, J. D.: Climatic and oceanographic isotopic signals from the carbonate rock record and their preservation, Geology Magazine, 129, 143–160, doi:10.1017/S0016756800008244, 1992.

Mayhew, P. J., Bell, M. a., Benton, T. G., and McGowan, A. J.: Biodiversity tracks temperature over time., Proceedings of the National Academy of Sciences of the United States of America, 109, 15 141–5, doi:10.1073/pnas.1200844109, http://www.pnas.org/content/109/38/15141, 2012.

Meyer, K., Kump, L., and Ridgwell, A.: Biogeochemical controls on photic-zone euxinia during the end-Permian mass extinction, Geology, 36, 747, doi:10.1130/G24618A.1, http://geology.gsapubs.org/cgi/doi/10.1130/G24618A.1, 2008.

Meyer, K., Yu, M., a.B. Jost, Kelley, B., and Payne, J.: δ^{13}C evidence that high primary productivity delayed recovery from end-Permian mass extinction, Earth and Planetary Science Letters, 302, 378–384, doi:10.1016/j.epsl.2010.12.033, http://linkinghub.elsevier.com/retrieve/pii/S0012821X10007958, 2011.

Meysman, F. J., Middelburg, J. J., Herman, P. M., and Heip, C. H.: Reactive transport in surface sediments. II. Media: an object-oriented problem-solving environment for early diagenesis, Computers & Geosciences, 29, 301–318, doi:10.1016/S0098-3004(03)00007-4, http://www.sciencedirect.com/science/article/pii/S0098300403000074, 2003.

Meysman, F. J. R., Risgaard-Petersen, N., Malkin, S. Y., and Nielsen, L. P.: The geochemical fingerprint of microbial long-distance electron transport in the seafloor, Geochimica et Cosmochimica Acta, 152, 122–142, doi:10.1016/j.gca.2014.12.014, http://dx.doi.org/10.1016/j.gca.2014.12.014, 2015.

Müller, P. J. and Suess, E.: Productivity, sedimentation rate, and sedimentary organic matter in the oceans-I. Organic carbon preservation, Deep Sea Research Part A, Oceanographic Research Papers, 26, 1347–1362, doi:10.1016/0198-0149(79)90003-7, http://www.sciencedirect.com/science/article/pii/0198014979900037?via{%}3Dihub, 1979.

Prokoph, A., Shields, G. a., and Veizer, J.: Compilation and time-series analysis of a marine carbonate d18O, d13C, 87Sr/86Sr and d34S database through Earth history, Earth-Science Reviews, 87, 113–133, doi:10.1016/j.earscirev.2007.12.003, 2008.

Pruss, S. B., Bottjer, D. J., Corsetti, F. a., and Baud, A.: A global marine sedimentary response to the end-Permian mass extinction: Examples from southern Turkey and the western United States, Earth-Science Reviews, 78, 193–206, doi:10.1016/j.earscirev.2006.05.002, http://linkinghub.elsevier.com/retrieve/pii/S0012825206000730, 2006.

R Core Team: R: A Language and Environment for Statistical Computing, https://www.r-project.org, 2016.

5 Rampino, M. R. and Caldeira, K.: Major perturbation of ocean chemistry and a 'Strangelove Ocean' after the end-Permian mass extinction, Terra Nova, 17, 554–559, doi:10.1111/j.1365-3121.2005.00648.x, http://onlinelibrary.wiley.com/doi/10.1111/j.1365-3121.2005.00648.x/abstract, 2005.

Reimers, C. E. and Suess, E.: The partitioning of organic carbon fluxes and sedimentary organic matter decomposition in the ocean, Marine Chemistry, 13, 141–168, doi:10.1016/0304-4203(83)90022-1, http://www.sciencedirect.com/science/article/pii/0304420383900221, 10 1983.

Reitner, J., Peckmann, J., Reimer, A., Schumann, G., and Thiel, V.: Methane-derived carbonate build-ups and associated microbial communities at cold seeps on the lower Crimean shelf (Black Sea), Facies, 51, 66–79, doi:10.1007/s10347-005-0059-4, http://www.sciencedirect.com/science/article/pii/S0025322701001281, 2005.

Renne, P. R., Black, M. T., Zichao, Z., Richards, M. a., and Basu, a. R.: Synchrony and causal relations between permian-triassic boundary 15 crises and siberian flood volcanism., Science, 269, 1413–1416, doi:10.1126/science.269.5229.1413, 1995.

Retallack, G. J. and Jahren, a. H.: Methane Release from Igneous Intrusion of Coal during Late Permian Extinction Events, The Journal of Geology, 116, 1–20, doi:10.1086/524120, http://www.jstor.org/stable/10.1086/524120, 2008.

Riccardi, A., Kump, L. R., Arthur, M. a., and D'Hondt, S.: Carbon isotopic evidence for chemocline upward excursions during the end-Permian event, Palaeogeography, Palaeoclimatology, Palaeoecology, 248, 73–81, doi:10.1016/j.palaeo.2006.11.010, http://linkinghub. 20 elsevier.com/retrieve/pii/S003101820600650X, 2007.

Richoz, S., Krystyn, L., Baud, A., Brandner, R., Horacek, M., and Mohtat-Aghai, P.: Permian–Triassic boundary interval in the Middle East (Iran and N. Oman): Progressive environmental change from detailed carbonate carbon isotope marine curve and sedimentary evolution, Journal of Asian Earth Sciences, 39, 236–253, doi:10.1016/j.jseaes.2009.12.014, http://linkinghub.elsevier.com/retrieve/pii/S1367912009002685, 2010.

25 Riding, R. and Liang, L.: Geobiology of microbial carbonates: metazoan and seawater saturation state influences on secular trends during the Phanerozoic, Palaeogeography, Palaeoclimatology, Palaeoecology, 219, 101–115, doi:10.1016/j.palaeo.2004.11.018, http://linkinghub.elsevier.com/retrieve/pii/S0031018204005930, 2005.

Ries, J. B., Anderson, M. A., and Hill, R. T.: Seawater Mg/Ca controls polymorph mineralogy of microbial $CaCO_3$: A potential proxy for calcite-aragonite seas in Precambrian time, Geobiology, 6, 106–119, doi:10.1111/j.1472-4669.2007.00134.x, http://onlinelibrary.wiley. 30 com/doi/10.1111/j.1472-4669.2007.00134.x/abstract, 2008.

Rothman, D. H., Fournier, G. P., French, K. L., Alm, E. J., Boyle, E. A., Cao, C., and Summons, R. E.: Methanogenic burst in the end-Permian carbon cycle., Proceedings of the National Academy of Sciences of the United States of America, 111, 5462–7, doi:10.1073/pnas.1318106111, http://www.pnas.org/content/111/15/5462.short, 2014.

Saltzman, M. R.: Late Paleozoic ice age; Oceanic gateway or pCO$_2$?, Geology, 31, 151–154, doi:10.1130/0091-7613(2003)031<0151, http: 35 //geology.gsapubs.org/content/31/2/151.abstract, 2001.

Sarmiento, J. L. and Gruber, N.: Calcium carbonate cycling, in: Ocean Biogeochemical Dynamics, chap. 9, pp. 1–44, Princeton University Press, New York, http://press.princeton.edu/titles/8223.html, 2004.

Schobben, M., Joachimski, M. M., Korn, D., Leda, L., and Korte, C.: Palaeotethys seawater temperature rise and an intensified hydrological cycle following the end-Permian mass extinction, Gondwana Research, 26, 675–683, doi:10.1016/j.gr.2013.07.019, http://linkinghub. elsevier.com/retrieve/pii/S1342937X13002694, 2014.

Schobben, M., Stebbins, A., Ghaderi, A., Strauss, H., Korn, D., and Korte, C.: Flourishing ocean drives the end-Permian marine mass
5   extinction, Proceedings of the National Academy of Sciences, 112, 10 298–10 303, doi:10.1073/pnas.1503755112, http://www.pnas.org/ lookup/doi/10.1073/pnas.1503755112, 2015.

Schobben, M., Ullmann, C. V., Leda, L., Korn, D., Struck, U., Reimold, W. U., Ghaderi, A., Algeo, T. J., and Korte, C.: Discerning primary versus diagenetic signals in carbonate carbon and oxygen isotope records: An example from the Permian–Triassic boundary of Iran, Chemical Geology, 422, 94–107, doi:10.1016/j.chemgeo.2015.12.013, http://linkinghub.elsevier.com/retrieve/pii/S0009254115301339, 2016.

10   Schobben, M., Stebbins, A., Algeo, T. J., Strauss, H., Leda, L., Haas, J., Struck, U., Korn, D., and Korte, C.: Volatile earliest Triassic sulfur cycle: A consequence of persistent low seawater sulfate concentrations and a high sulfur cycle turnover rate?, Palaeogeography, Palaeoclimatology, Palaeoecology, doi:10.1016/j.palaeo.2017.02.025, http://dx.doi.org/10.1016/j.palaeo.2017.02.025, 2017.

Schönbrodt, F.: Visually weighted/ Watercolor Plots, new variants: Please vote!, http://www.nicebread.de/, 2012.

Schrag, D. P., Higgins, J. a., Macdonald, F. a., and Johnston, D. T.: Authigenic carbonate and the history of the global carbon cycle., Science,
15   339, 540–543, doi:10.1126/science.1229578, http://www.ncbi.nlm.nih.gov/pubmed/23372007, 2013.

Soetaert, K. and Meysman, F.: Reactive transport in aquatic ecosystems: Rapid model prototyping in the open source software R, Environmental Modelling and Software, 32, 49–60, doi:10.1016/j.envsoft.2011.08.011, http://dx.doi.org/10.1016/j.envsoft.2011.08.011, 2012.

Soetaert, K., Herman, P. M. J., and Middelburg, J. J.: A model of early diagenetic processes from the shelf to abyssal depths, Geochimica et Cosmochimica Acta, 60, 1019–1040, doi:10.1016/0016-7037(96)00013-0, http://www.sciencedirect.com/science/article/
20   pii/0016703796000130, 1996.

Soetaert, K., Petzoldt, T., and Setzer, R.: Package deSolve: solving initial value differential equations in R, Journal of Statistical Software, 33, 1–25, doi:10.18637/jss.v033.i09, http://www.jstatsoft.org/v33/i09, 2010.

Soetaert, K., Petzoldt, T., and Meysman, F.: marelac: Tools for Aquatic Sciences, https://CRAN.R-project.org/package=marelac, r package version 2.1.6, 2016.

25   Song, H., Tong, J., Algeo, T. J., Horacek, M., Qiu, H., Song, H., Tian, L., and Chen, Z.-Q.: Large vertical $\delta^{13}C_{DIC}$ gradients in Early Triassic seas of the South China craton: Implications for oceanographic changes related to Siberian Traps volcanism, Global and Planetary Change, 105, 7–20, doi:10.1016/j.gloplacha.2012.10.023, http://linkinghub.elsevier.com/retrieve/pii/S0921818112002135, 2013.

Song, H., Tong, J., Algeo, T. J., Song, H., Qiu, H., Zhu, Y., Tian, L., Bates, S., Lyons, T. W., Luo, G., and Kump, L. R.: Early Triassic seawater sulfate drawdown, Geochimica et Cosmochimica Acta, 128, 95–113, doi:10.1016/j.gca.2013.12.009, http://linkinghub.elsevier.
30   com/retrieve/pii/S0016703713006935, 2014.

Svensen, H., Planke, S., Polozov, A. G., Schmidbauer, N., Corfu, F., Podladchikov, Y. Y., and Jamtveit, B.: Siberian gas venting and the end-Permian environmental crisis, Earth and Planetary Science Letters, 277, 490–500, doi:10.1016/j.epsl.2008.11.015, http://linkinghub. elsevier.com/retrieve/pii/S0012821X08007292, 2009.

Ullrich, T. S.: xyscan, http://rhig.physics.yale.edu/{~}ullrich/software/xyscan/, 2016.

35   van de Velde, S. and Meysman, F. J.: The influence of bioturbation on iron and sulphur cycling in marine sediments: a model analysis, Aquatic Geochemistry, 22, 469–504, doi:10.1007/s10498-016-9301-7, http://link.springer.com/article/10.1007/s10498-016-9301-7, 2016.

Veizer, J., Ala, D., Azmy, K., Bruckschen, P., Buhl, D., Bruhn, F., Carden, G. A. F., Diener, A., Ebneth, S., Godderis, Y., Jasper, T., Korte, C., Pawellek, F., Podlaha, O. G., and Strauss, H.: $^{87}Sr/^{86}Sr$, $\delta^{13}C$ and $\delta^{18}O$ evolution of Phanerozoic seawater, Chemical Geology, pp. 59–88, doi:10.1016/S0009-2541(99)00081-9.

Visscher, P. T., Reid, P. R., and Bebout, B. M.: Microscale observations of sulfate reduction: Correlation of microbial activity with lithified micritic laminae in modern marine stromatolites, Geology, 28, 919–922, doi:10.1130/0091-7613(2000)28<919:MOOSRC>2.0.CO, http://geology.gsapubs.org/content/28/10/919.full?sid=79e3865b-271f-4b2b-9d4d-484d9ec9c194, 2000.

Wacey, D., Wright, D. T., and Boyce, A. J.: A stable isotope study of microbial dolomite formation in the Coorong Region, South Australia, Chemical Geology, 244, 155–174, doi:10.1016/j.chemgeo.2007.06.032, http://www.sciencedirect.com/science/article/pii/S0009254107002586, 2007.

Wang, Y., Sadler, P. M., Shen, S. Z., Erwin, D. H., Zhang, Y. C., Wang, X. D., Wang, W., Crowley, J. L., and Henderson, C. M.: Quantifying the process and abruptness of the end-Permian mass extinction, Paleobiology, 40, 113–129, doi:10.1666/13022, http://paleobiol.geoscienceworld.org/content/40/1/113.abstract, 2014.

Wickham, H.: Reshaping Data with the reshape Package, Journal of Statistical Software, 21, 1–20, http://www.jstatsoft.org/v21/i12/, 2007.

Wickham, H.: ggplot2: Elegant Graphics for Data Analysis, Springer-Verlag New York, http://ggplot2.org, 2009.

Wickham, H.: The Split-Apply-Combine Strategy for Data Analysis, Journal of Statistical Software, 40, 1–29, http://www.jstatsoft.org/v40/i01/, 2011.

Wignall, P. B. and Twitchett, R. J.: Oceanic anoxia and the End Permian mass extinction, Science, 272, 1155–1158, doi:10.1126/science.272.5265.1155, http://science.sciencemag.org/content/272/5265/1155, 1996.

Winguth, A. M. E., Shields, C. A., and Winguth, C.: Transition into a Hothouse World at the Permian-Triassic boundary-A model study, Palaeogeography, Palaeoclimatology, Palaeoecology, 440, 316–327, doi:10.1016/j.palaeo.2015.09.008, http://dx.doi.org/10.1016/j.palaeo.2015.09.008, 2015.

Woods, A. D., Bottjer, D. J., Mutti, M., and Morrison, J.: Lower Triassic large sea-floor carbonate cements: Their origin and a mechanism for the prolonged biotic recovery from the end-Permian mass extinction, Geology, 27, 645, doi:10.1130/0091-7613(1999)027<0645:LTLSFC>2.3.CO;2, http://geology.gsapubs.org/content/27/7/645.abstract, 1999.

Xie, S., Pancost, R. D., Huang, J., Wignall, P. B., Yu, J., Tang, X., Chen, L., Huang, X., and Lai, X.: Changes in the global carbon cycle occurred as two episodes during the Permian-Triassic crisis, Geology, 35, 1083–1086, doi:10.1130/G24224A.1, http://geology.gsapubs.org/cgi/doi/10.1130/G24224A.1, 2007.

Xu, D.-Y. and Yan, Z.: Carbon isotope and iridium event markers near the Permian-Triassic boundary in the Meishan section, Zhejiang Province, China, Palaeogeography Palaeoclimatology Palaeoecology, 104, 171–176, doi:http://dx.doi.org/10.1016/0031-0182(93)90128-6, http://www.sciencedirect.com/science/article/pii/0031018293901286, 1993.

Yin, H., Jiang, H., Xia, W., Feng, Q., Zhang, N., and Shen, J.: The end-Permian regression in South China and its implication on mass extinction, Earth-Science Reviews, 137, 19–33, doi:10.1016/j.earscirev.2013.06.003, http://dx.doi.org/10.1016/j.earscirev.2013.06.003, 2014.

Zachos, J., Pagani, M., Sloan, L., Thomas, E., and Billups, K.: Trends, rhythms, and aberrations in global climate 65 Ma to present., Science, 292, 686–693, doi:10.1126/science.1059412, http://www.ncbi.nlm.nih.gov/pubmed/11326091, 2001.

Zeebe, R. E. and Westbroek, P.: A simple model for the CaCO$_3$ saturation state of the ocean; the "Strangelove," the "Neritan," and the "Cretan" ocean, Geochemistry, Geophysics, Geosystems, 4, 26 p., doi:10.1029/2003GC000538, http://doi.wiley.com/10.1029/2003GC000538, 2003.

Zhao, M.-Y., Zheng, Y.-F., and Zhao, Y.-Y.: Seeking a geochemical identifier for authigenic carbonate, Nature Communications, 7, 10 885, doi:10.1038/ncomms10885, http://www.nature.com/doifinder/10.1038/ncomms10885, 2016.

Zuo, J.-x., Tong, J.-n., Qiu, H.-o., and Zhao, L.-s.: Carbon isotope composition of the Lower Triassic marine carbonates, Lower Yangtze Region, South China, Science in China Series D: Earth Sciences, 49, 225–241, doi:10.1007/s11430-006-0225-8, http://link.springer.com/article/10.1007/s11430-006-0225-8, 2006.